HHS Public Access

Author manuscript

Nat Biomed Eng. Author manuscript; available in PMC 2024 June 09.

Published in final edited form as:

Nat Biomed Eng. 2024 May ; 8(5): 593–610. doi:10.1038/s41551-024-01194-7.

A synthetic cationic helical polypeptide as a multipotent innate immune activator for cancer immunotherapy

DaeYong Lee[1,2,*], **Kristin Huntoon**[1,2,*], **Yifan Wang**[3,*], **Minjeong Kang**[3], **Yifei Lu**[1,2], **Seong Dong Jeong**[1,2], **Todd M. Link**[4], **Thomas D. Gallup**[1,2], **Yaqing Qie**[1,2], **Xuefeng Li**[3], **Yifan Ma**[3], **Shiyan Dong**[3], **Benjamin R. Schrank**[3], **Adam Grippin**[3], **Abin Antony**[3], **Jonghoon Ha**[3], **Mengyu Chang**[3], **Yi An**[5], **Liang Wang**[3], **Dadi Jiang**[3], **Jing Li**[3], **Albert C. Koong**[3], **John A. Tainer**[4], **Wen Jiang**[3,#], **Betty Y.S. Kim**[1,2,#]

[1]Department of Neurosurgery, The University of Texas MD Anderson Cancer Center, Houston, TX, USA

[2]Brain Tumor Center, The University of Texas MD Anderson Cancer Center, Houston, TX, USA

[3]Department of Radiation Oncology, The University of Texas MD Anderson Cancer Center, Houston, TX, USA

[4]Department of Molecular and Cellular Oncology, The University of Texas MD Anderson Cancer Center, TX, USA

[5]Department of Therapeutic Radiology, Yale School of Medicine, CT, USA

Abstract

Intracellular DNA sensors regulate innate immunity and can provide a bridge to adaptive immunogenicity. However, activation of such sensors in antigen-presenting cells (APCs) by natural agonists such as double-stranded DNAs or cyclic nucleotides is impeded by several critical hurdles including poor intracellular delivery, serum stability, enzymatic degradation, and rapid systemic clearance. Here we engineered different polypeptides to influence their physicochemical properties and their ability to modulate immune responses via physical stress in APCs. We revealed that the optimal polypeptide was capable of activating two major intracellular DNA sensing pathways, toll-like receptor 9 (TLR9) and cyclic GMP–AMP synthase (cGAS)–stimulator of interferon genes (STING) preferentially in APCs by promoting the release of mitochondrial DNA. This subsequently led to efficient priming of effector T cells. The polypeptides exhibited potent innate immune sensor–mediated antitumor responses when given as monotherapy or

[#]Corresponding authors: Dr. Wen Jiang (wjiang4@mdanderson.org) and Dr. Betty Y.S. Kim (bykim@mdanderson.org).
[*]These authors contributed equally

Author contributions

D.Y.L., B.Y.S.K, and W.J. conceived the project and designed experiments. B.Y.S.K., and W.J. supervised the project. D.Y.L carried out all the experiments and analyzed all the data. Y.W., K.H., Y.L., M.K., SDJ, Y.Q. performed the *in vivo* studies. T.M.L and J.A.T. performed size exclusion chromatography for molecular weight determination. Y.W., X.L., S.D., Y.A., and J.L. helped to interpret the data. D.Y.L., W.J., and B.Y.S.K wrote the manuscript with the help from all authors.

Competing Interests

A provisional patent application based on the technology described in the manuscript has been filed by The University of Texas MD Anderson Cancer Center, with D.Y.L., K.H., W.J., and B.Y.S.K. as Inventors, Disclosure ID 03603.

Supplementary information

Supplementary Fig. 1-36, plus uncropped western blot images and gating strategies for flow cytometry

synergistically when given with T-cell checkpoint inhibitors, resulting in improved tumor control and prolonged survival in syngeneic mouse models of locally advanced and metastatic breast cancers. Collectively, these results demonstrate that the multipotent activation of innate immune sensing pathways via a cationic helical polypeptide-based immune modulator offers a promising therapeutic strategy to generate optimal antitumor immune responses.

Introduction

The innate immune system is crucial as a first line of host defense against pathogens or malignant transformation.[1,2] Antigen-presenting cells (APCs) such as dendritic cells (DCs) or macrophages act as an important bridge between innate and adaptive immune responses.[1-3] APCs can recognize and phagocytize transformed malignant cells, thereby promoting tumor-associated antigen presentation to induce cytotoxic effects in an antigen-specific manner.[1-3] Unfortunately, conditions within the tumor microenvironment often are capable of deactivating the immune surveillance capabilities of APCs by upregulating tumor-promoting factors such as immune checkpoints and anti-inflammatory cytokines and chemokines and altering the proportion of tumor-supporting cells.[4,5]

Activation of intracellular DNA sensing pathways such as cyclic GMP–AMP synthase (cGAS)–stimulator of interferon genes (STING) and/or toll-like receptor 9 (TLR9) can elicit tumor-specific cytotoxic T-cell immunity by upregulating type I interferon (IFN) responses.[6,7] Various strategies, including synthetic agonists with systemic activity[8-10], antibody-drug conjugates[11], nanoformulation of adjuvants for spatiotemporal delivery[12-15], and development of intrinsic STING-binding nanoparticles[16-18], have been devised to generate antitumor responses by stimulating such innate immune sensors. Despite their therapeutic promise in preclinical settings, successful demonstration of clinical utility of these agents have been limited. Therefore, investigations into new experimental compounds and platforms may broaden the pipeline of potential innate immune modulators that could ultimately result in patient benefit.

Distinct from the conventional design of agonist or delivery carriers, physical engineering of biomaterials can influence their physiochemical properties and enable regulation of immunogenicity in APCs in an unprecedented way.[19,20] By harnessing these phenomena, we hypothesized that engineering polypeptide physical characteristics would be able to induce immunogenicity with the desired physiochemical properties for enhanced cancer immunotherapy. Herein we set out to develop a new class of polypeptide-based agonists with systemic activity and immunogenicity preferentially within APCs by varying physical parameters such as hydrophobicity, electrostatic charges, and secondary conformation. Our findings suggest that polypeptide engineering with consideration of specific physical characteristics can modulate immunogenicity to implement efficient cancer immunotherapy.

Results

Engineering polypeptides to modulate antitumor immune responses.

Polypeptides are a platform that can be modulated in terms of their physiochemical properties, immunogenicity, and cellular and tissue penetrability by engineering distinct secondary structures and electrostatic charges.[21-23] To evaluate how these properties can be engineered through polypeptide design to achieve biological effects to be utilized in a therapeutic setting, we synthesized various polypeptides by altering their hydrophobicity, electrostatic charges, and structure of side chains (Supplementary Fig. 1-3). We first examined whether hydrophobicity of the polypeptide affected endoplasmic reticulum (ER) stress and mitochondrial DNA (mtDNA) release, two main regulators known to mediate key signaling pathways of innate immunity. We found that increasing the hydrophobicity of poly[4-(R-pentyloxy)benzoyl-L-lysine)] downregulated ER stress signaling and mtDNA release in bone marrow-derived macrophages (BMDMs) (Extended Fig. 1a-c). Interestingly, the cyclic amine-tethered polypeptides more favorably induced ER stress and mtDNA release than did the linear counterparts (Extended Fig. 1a-c). We also aimed to determine whether hydrophobicity in polypeptide designs could also modulate pro-inflammatory responses and effector functions specifically in APCs via ER stress-mediated mtDNA release. Consistent with our prior results, we found that polypeptides with hydrophilicity and cyclic amines more strongly increased the expression of genes encoding pro-inflammatory cytokines, phagocytosis of EO771 tumor cells, and antigen presentation of ovalbumin (OVA) peptide (Extended Fig. 1d-f). Next, we assessed whether modifying electrostatic charges via polypeptide engineering would modulate ER stress and mtDNA release to affect pro-inflammatory responses and effector functions in APCs. We first tested whether their cationic properties would induce ER stress and mtDNA release in BMDMs. As expected, P1 and phenyltrimethylammonium (PTMA) (a strong polycation) stimulated ER stress and promoted mtDNA release relative to polystyrene (PS) (a strong anion) (Extended Fig. 2a-c). We further evaluated pro-inflammatory responses and effector functions in APCs by treating BMDMs with P1, PTMA, and PS. P1 was found to generate profound pro-inflammatory responses, enhanced phagocytosis of cancer cells, and cross-presentation of OVA to a greater extent than did PTMA and PS (Extended Fig. 2d-f). In the last step, we verified whether the chain structure of polypeptides would influence immunogenicity and effector functions in APCs via ER stress-mediated mtDNA release. We first evaluated whether elongating the side chains of the polypeptides would induce ER stress and mtDNA release in APCs (Extended Fig. 3a-c), and found that polypeptides with extended side chains more favorably activated ER stress and mtDNA release in APCs. Similarly, the polypeptides with elongated side chains also led to enhanced generation of pro-inflammatory responses, phagocytosis of EO771 tumor cells, and antigen presentation of OVA in BMDMs (Extended Fig. 3d-f). With these experimental results, we selected the three top-performing polypeptides (P1, P2, P3) for further optimization, as described below.

We sought to further optimize the cationic polypeptide structures that were bio-applicable by characterizing their physiochemical properties *in vitro*. Although none of the polypeptides induced cytotoxicity or proteolytic degradation, P1, with its helicity structure and ethylene glycol moieties, showed better serum stability (Supplementary Fig. 4,5). Next, we set out

to determine the biodistribution of the cationic polypeptides after systemic administration *in vivo* by injecting fluorophore-tagged P1, P2, and P3 (Fig. 1a) into mice. The near-infrared fluorescence signal of P1 and P2 remained in the whole body over long periods, whereas that of P3 was rapidly attenuated (Fig. 1b-d). Pharmacokinetics assays indicated that P1 remained in circulation in the mouse body for longer periods than P2 and P3 (Fig. 1e). P1 also accumulated in deeper regions of the EO771 tumors to a greater extent than did P2 and P3 (Supplementary Fig. 6). We conclude from these experimental outcomes that the polypeptide structure of P1 provided high systemic activity *in vivo,* thus increasing its passive accumulation in tumor. Further analyses of fluorescence signals within tumors showed that P1 accumulated more in $CD45^+$ cells than in $CD45^-$ epithelial cellular adhesion molecule $(EpCAM)^+$ cells[24] and at higher levels compared with P2 and P3 (Fig. 1f and Supplementary Fig. 7). In addition, among $CD45^+$ cells, tumor-homing macrophages and dendritic cells (DCs) took up the most of cationic polypeptide, suggesting that a cationic helical polypeptide could specifically stimulate tumor-infiltrating APCs (Fig. 1g,h and Supplementary Fig. 7).

Next, we set out to determine the optimal dose of polypeptide, in terms of systemic activity. P1 suppressed tumor growth and extended mouse survival in a dose-dependent manner at doses up to, but not beyond, 20 mg/kg (Supplementary Fig. 8,9). We further characterized the toxicological properties of P1 to verify its applicability *in vivo*. P1 did not induce cytotoxicity in breast cancer cells or APCs *in vitro* (Supplementary Fig. 10). Although P1 treatment induced transient inflammation in liver-resident macrophages and peripheral blood plasma, inflammation-mediated toxicity in organs and peripheral blood cells was not observed (Supplementary Fig. 11-16). Next, we evaluated the antitumor and immune effects of P1, P2, and P3 in EO771 tumor-bearing mice (Fig. 1i). Treatment with P1 slowed the growth rate of EO771 tumors and extended survival to a greater extent than did P2 and P3 (Fig. 1j). Assessment of adaptive immune cell profiles after treatment with P1 demonstrated significant increases in $CD8^+$ T cells and IFN-γ-producing $CD8^+$ T cells within the tumor relative to treatment with P2 or P3 (Extended Fig. 4a). In addition, evaluation of tumor-homing myeloid cell populations showed that P1 treatment promoted pro-inflammatory macrophage polarization and DC maturation to a greater extent than did P2 and P3, but the population of myeloid-derived suppressor cells (MDSCs) within the tumor was maintained regardless of treatment (Extended Fig. 4b). From these experimental outcomes, we conclude that cationic polypeptides with high helicity and serum stability not only improve systemic activity but also generate favorable antitumor immunity in solid tumors.

We also compared the antitumor immune effects of P1 with those of two pathogen recognition receptor–specific agonists, CpG oligodeoxynucleotides (CpG) and cyclic GMP-AMP (cGAMP) (Fig. 2a). Treatment with P1 induced stronger tumoricidal effects and extended mouse survival relative to treatment with CpG and cGAMP (Fig. 2b-d). Analyses of tumor-infiltrating lymphocytes and their subtypes by flow cytometry demonstrated that P1 treatment increased the population of $CD8^+$ T cells and IFN-γ^+CD8^+ T cells but reduced the population of regulatory T cells (Tregs) relative to CpG and cGAMP treatment (Fig. 2e). Further investigation of myeloid cells showed that P1 treatment promoted M1 macrophage polarization and DC maturation while maintaining the MDSC population (Fig. 2f). Next, using immunofluorescence we observed that P1 triggered tumor infiltration by

both $CD4^+$ and $CD8^+$ T cells and increased the expression of ionized calcium-binding adaptor molecule (Iba) 1, which is associated with phagocytosis activation, relative to CpG and cGAMP (Fig. 2g). We also tested whether P1 treatment would induce memory effects in splenic T cells and systemic inflammatory responses. Evaluation of memory T-cell subtypes and inflammatory cytokines showed that P1 induced both effector and central memory phenotypes in splenic T cells and increased serum levels of interleukin (IL)-2 and IFN-γ to a greater extent than did CpG and cGAMP (Supplementary Fig. 17).

To evaluate the therapeutic potency of P1, we performed head-to-head comparison studies between P1 and commercially available agonists including ADU-S100 and MSA-2, or combined CpG and cGAMP (Fig. 2h). P1 suppressed the growth of EO771 tumors and extended the survival period of tumor-bearing mice relative to ADU-S100, MSA-2, or cGAMP+CpG (Fig. 2i). On the basis of these experimental results, we conclude that P1 could represent a new class of immunostimulatory molecule and a potential systemic agonist to induce antitumor immune responses.

P1 stimulates intracellular DNA sensors in APCs.

To determine the effect of P1 specifically on APCs, we first quantified the expression of macrophage phenotypic markers and type I IFNs after treatment with this cationic helical polypeptide. P1 upregulated M1-related genes and also type I IFN-associated genes, and downregulated M2-related genes, in M2 macrophages compared with untreated controls (Fig. 3a and Supplementary Fig. 18). M2-related *cd206* and *chil3*, but not *arg1* or *il10*, were remarkably reduced after a 24-hour incubation with P1 (Fig. 3a and Supplementary Fig. 18). We also found that treating bone marrow-derived DCs (BMDCs) with P1 significantly elevated the expression of genes for pro-inflammatory cytokines and co-stimulatory molecules relative to untreated controls (Fig. 3b).

Given that APC activation can be triggered by agonizing innate immune sensors,[25-27] we next assessed whether P1 activated these pathways in APCs. As expected, P1 activated both the cGAS-STING-interferon regulatory factor (IRF) 3 and myeloid differentiation primary response 88 (MyD88)-IRF7 axes as well as their downstream canonical nuclear factor κ B (NF-κB) pathway in APCs (Fig. 3c and Supplementary Fig. 19). Collectively, these findings suggest that this cationic polypeptide exerted its pro-inflammatory effects on APCs via several independent pathways.

To further elucidate the mechanisms involved in cationic helical polypeptide–mediated immune activation in APCs, we first set out to identify the cellular compartment in which they stimulate innate immune sensors. Fluorescently labeled P1 was initially retained in lysosomes but was ultimately trafficked to the ER but not to mitochondria (Supplementary Fig. 20). Also, treating BMDMs with P1 transiently disrupted the integrity of lipid plasma membranes in lysosomes (Supplementary Fig. 21). The ability of P1 to physically disrupt lysosomes and accumulate in the ER suggests that P1 would likely generate ER stress in APCs. Indeed, we found that P1-induced physical stress in BMDMs increased intracellular reactive oxygen species (ROS) levels and then exerted ER stress, thus triggering mtDNA release (Supplementary Fig. 22). To further test whether P1-mediated ER stress induction affected mtDNA release in APCs, we visualized the release of DNA and mitochondrial

transcription factor A (TFAM), which binds to mtDNA, from mitochondria in macrophages. We observed that P1-exposed BMDMs promoted the release of DNA and TFAM from mitochondria (Fig. 3d). Further measurement of mitochondrial ROS and cytosolic mtDNA DNA levels showed that P1-exposed APCs generated mitochondrial ROS and also promoted mtDNA release from their cytosol (Fig. 3e and Supplementary Fig. 23).

Because ER stress-mediated mtDNA release can activate both cGAS-STING and TLR,[7,28] we next assessed whether this also occurred after P1 treatment. Knockout of MyD88 or STING in P1-exposed macrophages or DCs led to downregulation of inflammation-related genes and de-activation of MyD88-IRF7 and STING-IRF3, respectively (Fig. 3f,g). However, deficiency of MyD88 more strongly suppressed the canonical NF-κB pathway than did knockout of STING (Fig. 3g). We further assessed pro-inflammatory signaling by using $cGAS^{-/-}$ APCs to determine whether P1-mediated upregulation of type I IFN responses was attributable to cGAS activation. Treating $cGAS^{-/-}$ APCs with P1 attenuated type I IFNs responses by de-activating the STING-IRF3 axis (Supplementary Fig. 24). These findings led us to conclude that P1 treatment indirectly stimulated both cGAS-STING and TLR pathways to propagate pro-inflammatory responses.

Because P1 was noted to mediate self/foreign DNA stimulation of TLR9, we hypothesized that P1 was likely to stimulate TLR9.[7, 28] We used several assays to demonstrate that treating APCs with P1 promoted the release of mtDNA from the cytosol, after which the neighboring APCs took up the extracellular mtDNA, thereby activating TLR9 signaling via an autophagic process (Supplementary Fig. 25). Next, we quantified expression of inflammation-related genes and proteins related to TLR pathways by using $TLR9^{-/-}$ APCs. Treating these TLR9-deficient macrophages or DCs with P1 reduced the expression of genes corresponding to pro-inflammatory cytokines and deactivated the MyD88-IRF7 and canonical NF-κB pathways (Fig. 3h,i). We further confirmed that P1-induced immunogenicity was not associated with the TLR3-TIR-domain-containing adapter-inducing interferon-β (TRIF) axis for RNA sensing (Supplementary Fig. 26).[29]

Activation of the TLR9 or STING pathways is known to stimulate NLR family pyrin domain containing 3 (NLRP3) inflammasomes as a downstream pathway.[30,31] Therefore we examined whether P1 treatment agonized this pathway. P1 was found to stimulate the NLRP3 inflammasome axis and also produced the corresponding marker IL-1β; in combination with priming with lipopolysaccharide (LPS), P1 strongly upregulated the NLRP3 inflammasome cascade and also boosted secretion of IL-1β in APCs (Supplementary Fig. 27). We further tested whether P1 with LPS priming activated the NLRP3 inflammasome axis in both a cGAS- and STING-dependent manner. Deficiency of cGAS and STING in APCs reduced the expression of NLRP3 and cleaved caspase 1 and the secretion of IL-1β (Supplementary Fig. 28). These experimental results suggest that P1 first indirectly activated both the TLR9 and cGAS-STING axes by mtDNA release, and then consecutively stimulated NLRP3 inflammasome signaling, thus propagating a pro-inflammatory response.

We next tested whether P1 treatment affects propagation of pro-inflammatory responses via ER stress-mediated mtDNA release in cancer cells. P1 treatment did not induce

ER stress-mediated mtDNA release in either EO771 and 4T1 breast tumor cells, and thus were unlikely to induce pro-inflammatory responses via cGAS-STING or TLR axes (Supplementary Fig. 29). We also examined whether P1 affects the expression of immune checkpoints or induces immunogenic cell death. Investigation of the associated markers verified that treating breast cancer cells with P1 did not change the expression of immune checkpoints or the release of damage-associated molecular patterns (Supplementary Fig. 30).

P1 increases phagocytosis of cancer cells and downstream immune activation by APCs.

To assess how the cationic polypeptide affects the effector functions of APCs, we treated M2-polarized macrophages co-cultured with breast cancer cells with the polypeptide and corresponding controls. P1 treatment consistently increased tumor cell phagocytosis by macrophages or DCs relative to the other treatments (Fig. 4a,b and Supplementary Fig. 31). We next tested whether the cationic polypeptide could also promote antigen cross-presentation by APCs after tumor cell phagocytosis. As expected, P1 treatment resulted in increased cross-presentation of the OVA peptide by the major histocompatibility protein (MHC) I complex (Fig. 4b,c). P1 treatment of APCs co-cultured with EO771 breast cancer cells also promoted the production of pro-inflammatory cytokines (Fig. 4d,e), many of which are essential for the efficient priming of T cells.[32,33]

To determine whether P1-activated APCs can more efficiently prime antigen-specific T cells, we incubated macrophages or DCs that had previously been co-cultured with OVA-expressing EO771 cells with $CD4^+$ or $CD8^+$ T cells from OT-II and OT-I transgenic mice, respectively. P1 treatment was found to increase the proliferation of both OT-I and OT-II T cells (Fig. 4f). Moreover, the cationic polypeptide treatment promoted a shift toward memory phenotypes in both $CD4^+$ and $CD8^+$ T cells (Fig. 4g,h). These results suggest that the cationic polypeptide can promote APC activation and tumor cell phagocytosis, leading to enhanced tumor antigen cross-presentation and subsequent priming of memory T cells.

P1 synergizes with T-cell checkpoint inhibitor.

Activation of innate antitumor immune responses can result in adaptive immune resistance.[1] Therefore, we assessed whether treatment with the cationic polypeptide P1 increased the expression of programmed cell death 1 (PD1) and programmed cell death ligand 1 (PDL1) on immune cells and tumor cells, respectively. We found that P1-induced innate immune activation triggered upregulation of PD1 expression on tumor-infiltrating DCs, macrophages, and T cells and upregulation of PDL1 on EO771 tumor cells (Supplementary Fig. 32). To overcome this adaptive immune resistance, we sought to confirm whether adding a T-cell immune checkpoint blocker, anti-programmed cell death 1 (αPD1), would synergistically improve tumor-suppressing effects in mice with locally advanced and metastatic breast tumors (Fig. 5a and Extended Fig. 5a). The combination of αPD1 and P1 suppressed tumor proliferation and also extended the survival of tumor-bearing mice to a greater extent than did P1 or αPD1 as monotherapy, or cGAMP+αPD1, in both 4T1- and EO771-tumor–bearing models (Fig. 5b-d and Extended Fig. 2b-d), even in mice with large EO771 tumors (Supplementary Fig. 33).

Next, we examined whether P1+αPD1 treatment affected recruitment of tumor-infiltrating lymphocytes into tumors. P1+αPD1 treatment increased total tumor-infiltrating $CD45^+$ cells compared with the other treatments (Supplementary Fig. 34). Further investigation of immune cell subtypes within the tumor microenvironment confirmed that P1+αPD1 treatment improved the infiltration of T cells, macrophages, and DCs into the tumors relative to the other treatments (Supplementary Fig. 34). These results indicate that combining P1 and immune checkpoint blockade enhanced therapeutic responses by increasing the immune populations within the tumor microenvironment.

Next, we evaluated adaptive immune cell profiles after P1+αPD1 combination therapy. We found significant increases in both $CD4^+$ and $CD8^+$ T cells within the tumor as compared with treatment with P1, αPD1, or cGAMP+αPD1 (Fig. 5e,f and Extended Fig. 5e,f). Further analyses of T-cell subsets confirmed that numbers of tumor-infiltrating IFN-γ^+CD8^+ T cells were elevated, and the population of Tregs was reduced, after P1+αPD1 combination therapy compared with P1, αPD1, or cGAMP+αPD1 treatment (Fig. 5e and Extended Fig. 5e). In addition, investigation of tumor-homing myeloid cell populations demonstrated that the P1+αPD1 combination treatment triggered M1 macrophage polarization, DC maturation, and Iba1 upregulation, but decreased the population of tumor-associated MDSCs, to a greater extent than the other treatments (Fig. 5f,g and Extended Fig. 5f,g). We further tested whether P1+αPD1 treatment led to tumor-specific T-cell responses in mice bearing EO771-expressing OVA in cytosol (EO771-cOVA) tumors (Fig. 5h). Analysis of the OVA tetramer in $CD8^+$ T cells showed that P1+αPD1 treatment promoted the generation of OVA-specific $CD8^+$ T cells within the tumor and spleen (Fig. 5i,j), suggesting that P1+αPD1 treatment efficiently elicited tumor-specific T-cell responses to induce cytotoxic killing in a systemic manner (Fig. 5k).

To assess whether P1+αPD1 treatment could evoke systemic immune responses, we next analyzed immune cell subtypes in spleen and tumor-draining lymph nodes. Our assessment of T-cell subpopulations in tumor-draining lymph nodes demonstrated that $CD8^+$ T cells produced IFNγ, and the number of Tregs was reduced after P1+αPD1 treatment compared with the other treatments (Extended Fig. 6a). Also, investigation of myeloid populations in spleen and tumor-draining lymph nodes showed that P1+αPD1 treatment promoted pro-inflammatory macrophage polarization and DC maturation to a greater extent than did the other treatments (Extended Fig. 6b). On the other hand, P1+αPD1 treatment reduced the population of MDSCs in spleen but not in tumor-draining lymph nodes (Extended Fig. 6b). Next, we also examined whether P1+αPD1 treatment generated memory effects in splenic T cells and systemic immune responses. Assessment of memory T-cell subtypes and inflammatory cytokines showed that P1+αPD1 induced both effector and central memory phenotypes in splenic T cells as well as increasing IL-2 and IFN-γ in serum (Supplementary Fig. 35, 36). Together, these results demonstrate that P1, given with a T-cell checkpoint inhibitor, shifted the immune profile toward a tumor-suppressive state, thereby generating robust systemic antitumor immune responses.

P1 combined with αPD1 elicits antitumor immunity by activating innate immune sensors.

We next investigated whether P1+αPD1 antitumor immunity effects are mediated by activation of STING and TLR9-MyD88. We found that deficiency in STING, MyD88, or TLR9 not only abolished the tumor-inhibitory effects of P1+αPD1 but also reduced the survival of tumor-bearing mice (Fig. 6a,b). Further evaluation of type I IFN gene expression in APCs revealed that the P1+αPD1 treatment significantly increased expression of the corresponding mRNAs in tumors from WT but not from STING$^{-/-}$, MyD88$^{-/-}$, or TLR9$^{-/-}$ mice (Fig. 6c). We next examined whether P1+αPD1 treatment triggered nuclear translocation of phosphorylated IRF3 (p-IRF3) or p-IRF7 via TLR9-MyD88 and STING signaling to generate type I IFN responses.[2,6,34] Immunofluorescence analysis of p-IRF3 in tumor-resident APCs showed that P1+αPD1 triggered nuclear translocation of p-IRF3 in APCs in WT mice but not in STING$^{-/-}$ or MyD88$^{-/-}$ mice (Fig. 6d,e and Extended Fig. 7). Regarding p-IRF7 in tumor-homing APCs, TLR9$^{-/-}$ macrophages and DCs showed blocked nuclear translocation of p-IRF7 even in the presence of P1+αPD1 (Extended Fig. 8a). These experimental outcomes collectively demonstrate that propagation of both TLR9-MyD88 and STING signaling pathways is required to generate P1+αPD1-mediated antitumor responses by activating type I IFNs responses.

Considering that type I IFNs have key roles in recruiting cytotoxic T cells within tumors[32,33], we next visualized tumor-infiltrating T cells by immunofluorescence staining. Knockout of STING, MyD88, and TLR9 all abrogated the recruitment of CD8$^+$ and CD4$^+$ T cells within tumors in the P1+αPD1–treated mice (Fig. 6f,g and Extended Fig. 8b), implying that activation of STING and TLR9-MyD88 signaling is crucial for P1+αPD1–mediated activation of adaptive immunity.

To identify whether activation of STING and MyD88 in tumors is required for P1+αPD1–mediated antitumor responses, we established EO771 STING$^{-/-}$ and MyD88$^{-/-}$ cells via clustered regularly interspaced short palindromic repeats (CRISPR) gene editing (Extended Fig. 9a), and then inoculated the EO771 WT, EO771 STING$^{-/-}$, and EO771 MyD88$^{-/-}$ cells into C57/BL6 mice. Deficiency in either innate immune sensor in breast cancer cells did not affect tumor growth or survival of tumor-bearing mice treated with P1+αPD1 (Extended Fig. 9b). These results clearly demonstrate that stimulation of both STING and MyD88 in host cells is essential to generate P1+αPD1-based antitumor immunity.

P1 combined with αPD1 promotes innate and adaptive antitumor immune responses.

To verify whether activation of innate immunity is required for P1+αPD1–mediated immunotherapy, we depleted macrophages and DCs in EO771 tumor-bearing mice by using a colony-stimulating factor 1-receptor antibody (αCSF1-R) in WT mice and diphtheria toxin in CD11c-diphtheria toxic receptor (DTR) transgenic mice, respectively. Depletion of macrophages or DCs abolished the antitumor effect of P1+αPD1 and reduced the survival of EO771 tumor-bearing mice (Fig. 7a). Analysis of tumor-infiltrating lymphocytes revealed that deficiency of macrophages or DCs in the P1+αPD1 treatment group reduced the number of tumor-infiltrating CD8$^+$ T cells and macrophages in αCSF1-R-treated mice, and DCs in CD11c-depleted mice (Fig. 7b,c). Further analyses of myeloid cells confirmed that DC maturation and M1 macrophage polarization in the P1+αPD1 group were inhibited in

the DC-depleted and macrophage-depleted mouse models, respectively, but the proportion of MDSCs was increased (Fig. 7d). Next, assessment of T-cell subtypes revealed that depletion of macrophages or DCs in P1+αPD1–treated mice led to deactivation of effector $CD8^+$ T cells but increased the proportion of Tregs. We conclude that activation of innate immunity by P1+αPD1 is required to remodel the tumor microenvironment toward an immune-activating mode.

To examine whether the antitumor effect of P1+αPD1 depends mainly on $CD8^+$ T cell–mediated adaptive immunity, we depleted $CD8^+$ T cells in EO771 tumor-bearing mice by using αCD8 (Extended Fig. 10a). CD8 depletion completely abrogated the antitumor immunity conferred by P1+αPD1 and also shortened the survival of mice with EO771 tumors (Extended Fig. 10b-d). The tumor-infiltrating T-cell profile in the P1+αPD1 group revealed that CD8 depletion not only blocked recruitment of $CD8^+$ T cells but also decreased the production of IFN-γ from $CD8^+$ T cells while maintaining Treg proportions (Extended Fig. 10e,f). These experimental outcomes show that the tumoricidal effect of P1+αPD1 treatment relied mainly on $CD8^+$ T cell–mediated cytotoxicity.

P1 combined with αPD1 suppresses aggressive tumor metastasis.

Residual tumors or circulating tumor cells can cause recurrence and metastasis even after surgical resection of the primary tumor.[35] We established BR4, a 4T1-brain-tropic (4T1-BR4-Luc), aggressive metastatic breast cancer cell line, and tested whether P1 combined with αPD1 would be effective in treating these aggressive metastatic tumors. We first generated a spontaneous metastasis model by inoculating 4T1-BR4-Luc cells into mice and resecting the resulting tumors on day 14 (Fig. 8a). Using bioluminescence imaging to track the 4T1-BR4-Luc *in vivo,* we discovered that P1+αPD1 treatment suppressed tumor metastasis for longer than the other treatment conditions (Fig. 8b-d). Moreover, two of the eight mice in the P1+αPD1 treatment group were tumor-free and survived up to day 150 (Fig. 8c,d).

We further examined whether P1+αPD1 treatments established tumor-specific memory in a spontaneous metastasis model (Fig. 8e). We first treated mice that had spontaneous metastases with HEPES or P1+αPD1, and then monitored survival afterward; 6 of the 14 mice treated with P1+αPD1 survived until day 65, whereas all the mice treated with HEPES died (Fig. 8f). Next, we re-challenged naïve (unimmunized) and the mice with long-term survival (up to 65 days) with 4T1-BR4 to verify the generation of tumor-specific memory in the P1+αPD1 (immunized group). As expected, the mice with long-term survival showed suppressed 4T1-BR4 tumor growth and extended survival compared with the naïve group (Fig. 8g). Taken together, these findings indicate that the P1+αPD1 combination was much more effective for treating these aggressive metastatic tumors and establishing tumor-specific memory.

Discussion

We present a new physical engineering approach to eliciting antitumor immunity by stimulating innate immune sensors with systemic activity. Engineering the physical properties of polypeptides allowed us to modulate innate immunogenicity specifically

in APCs by stimulating intracellular DNA sensors and modifying the physicochemical properties of the polypeptides. Mechanistically, P1, the optimal polypeptide, activated the intracellular DNA sensors cGAS and TLR9 via ER stress-mediated mtDNA release in APCs, thereby generating pro-inflammatory responses in APCs. The P1-exposed APCs promoted phagocytosis of cancer cells and processing of presented antigens, thereby priming tumor-specific T cells.

Accumulating preclinical evidence that adjuvant-based cancer immunotherapy has strong potential for clinical translation[6,36] led us to propose that activation of innate immunity would be a promising way to implement efficient cancer immunotherapy. In terms of clinical applicability, small molecule-based innate immune agonists (e.g., ADU-S100, MK-1454, SD-101) have been found to induce less potent antitumor responses and to have dose-limiting toxicity in clinical trials, which would be associated with unsatisfactory bioavailability and pharmacologic activity[37-39]. On the other hand, polymeric innate immune agonists were found to be capable of sensitizing or prolonging pro-inflammatory responses via multivalent interactions with innate immune sensors (e.g., PC7A[17] or polymeric CpG[40]) or indirection stimulation of innate immune signaling (e.g., chitosan[41]). Despite their promise in immuno-oncology applications, some of these polymeric agonists cannot be administered systemically or are potentially toxic because of their non-specific stimulation of innate immune sensors, thus likely limiting their clinical applicability.

With the goal of improving the functionalities of polymer-based agonists, we first devised a physical engineering strategy for modulating the immunogenicity and pharmacologic activity of polymer-based immune stimulants. Distinct from the previous approaches, serial optimizations of polypeptide libraries via physical engineering facilitated regulation of innate immune responses and pharmacologic properties. Indeed, the optimal polypeptide-based innate immune adjuvant P1 not only preferentially targeted APCs rather than non-immune cells or T cells but also selectively generated pro-inflammatory responses in APCs by controlling ER stress signaling without adverse effects. Given the significance of stimulating innate immune sensors specifically in APCs[42-44], our molecular design of P1 enables selective activation of innate immune signaling in APCs, thereby providing a novel strategy for implementing efficient cancer immunotherapy.

Although our findings support the proposition that physically engineering polypeptides can enhance their potential usefulness in cancer immunotherapy, we found that P1 produced modest therapeutic benefit in treating locally advanced solid tumors. Regardless, our study opens up a new avenue of investigations for polypeptide engineering in the context of cancer immunotherapy that could be expanded to other disease settings, where further investigations of physiochemical attributes such as chirality, molecular weight and multivalency may continue to improve the therapeutic index of new polypeptide designs.

Methods

Synthesis

Poly-(4-(5-chloropentyloxy)benzoyl-L-lysine)) and poly (4-(chloromethyl)benzoyl-L-lysine) were prepared according to previously published procedures.[45-47] Poly(3-

chloropropinoyl-L-lysines) were synthesized by carbodiimide chemistry. Briefly, 3-chloroproionyl acid were converted to *N*-hydroxysuccinimide ester by using *N*-Ethyl-*N*′-(3-dimethylaminopropyl)carbodiimide hydrochloride and *N*-hydroxysuccnimide in dimethylformamide (DMF) (20 mL) for 3 h before poly-L-lysine (0.2 g in 5 mL deionized water) were added to proceed the coupling reaction at RT for 2 days. Poly(3-chloropropionyl-L-lysine was isolated by precipitation with excess deionized water, and then free-dried to obtain a white powder (0.18 g).

For the hydrophobicity optimization step, Poly-(4-(5-chloropentyloxy)benzoyl-L-lysine)) (0.1 g) was dissolved in anhydrous DMF (10 mL) with triethylamine (296 μL, 2.27 mmol) before the addition of dimethyl amine (61 μL, 0.91 mmol [TCI, Tokyo, Japan]) for PDM, diethyl amine (101 μL, 0.91 mmol [TCI]) for PDE, dibutyl amine (101 μL, 0.91 mmol [TCI]) for PDB, 4-methyl piperidine (153 μL, 0.91 mmol [TCI]) for PP, 1-hydroxyethylethoxy piperazine (0.16 g, 0.91 mmol [TCI]) for P1 and 1-methylpiperazine (111 μL, 0.91 mmol [TCI]) for P2.

To modify the electrostatic charge, poly-(4-(5-chloropentyloxy)benzoyl-L-lysine)) (0.1 g) was first reacted with NaI (0.136 g, 0.91 mmol, Fisher Scientific) to convert chloride to iodide before trimethyl amine (1 mL, 3 mmol in 1 M trimethylamine THF solution [TCI]) for phenyltrimethylammonium (PTMA) and sodium sulfite (0.344 g, 2.73 mmol, TCI) for polystyrene (PS) were added to continue the reaction.

For optimizing side chain length, poly-(4-(chloromethyl)benzoyl-L-lysine) (0.1 g) or poly(3-chloropropionyl-L-lysine) solubilized in DMF and triethylamine was mixed with 1-hydroxyethylethoxy piperazine (0.16 g, 0.91 mmol) to synthesize P3 and PHP, respectively. The S_N2 reaction for all the polypeptides was allowed to proceed at 100°C for 1 day. The reaction mixture was precipitated with diethyl ether. The crude products were solubilized in 0.1 N HCl excluding PTMA and PS. The solution was dialyzed against deionized water to remove the unreacted reagent or salts and then lyophilized to obtain P1 (0.12 g), P2 (0.13 g), P3 (0.09 g), PTMA (0.1 g), PS (0.05 g), PP (0.11 g), PDM (0.09 g), PDE (0.11 g), PDB (0.13 g), and PHP (0.04 g).

Cell lines

THP-1, EO771, TUBO, 4T1, and SK-BR3 breast cancer cell lines were purchased from the American Type Culture Collection and maintained in Dulbecco's minimum essential medium (DMEM) supplemented with 10% fetal bovine serum (FBS), 1% sodium pyruvate, 1% penicillin/streptomycin, and 0.2% Normocin. The 4T1 cell line was transfected with lentivirus encoding firefly luciferase gene to establish 4T1-Luc. 4T1-BR4-Luc cells were developed after four rounds of intracardiac injection/brain cell culture. EO771 STING$^{-/-}$ and EO771 MyD88$^{-/-}$ cell lines were established by using CRISPR gene editing kits (Origene, USA). Knockout of STING or MyD88 in EO771 cells was established according to the manufacturer's guidelines. EO771-cOVA cells were developed by pLenti-cOVA transfection according to a previous protocol.[48]

Preparation of antigen-presenting cells

Bone marrow-derived macrophages (BMDMs) and bone marrow-derived dendritic cells (BMDCs) were prepared from the femur and tibia of 6- to 10-week-old C57BL/6 mice bred at MD Anderson Cancer Center or The Jackson Laboratory. Balb/C mice, *MyD88*-knockout mice (The Jackson Laboratory, USA), *TLR9*-knockout mice, *cGAS*-knockout mice, and *tmem173*^{gt} mice (all from The Jackson Laboratory, USA) were established according to a previous protocol.[40] BMDMs were maintained in DMEM supplemented with a 30% L929 cell-conditioned medium (Stony Brook Cell Culture/Hybridoma facility), 20% FBS, 1% sodium pyruvate, and 1% penicillin/streptomycin. M2 macrophages were prepared by exposing BMDMs to IL-4 (10 ng/mL) for 2 days. For BMDC differentiation, monocytes from bone marrow were differentiated in cell culture medium including granulocyte-macrophage colony stimulating factor (20 ng/mL) and IL-4 (10 ng/mL) for 10 days. For THP-1 macrophage differentiation, THP-1 cells were treated with 200 nM phorbol 12-myristate 13-acetate for 3 days and then incubated without phorbol 12-myristate 13-acetate for another 2 days to obtain human macrophage-like cells.

Reverse transcription quantitative polymerase chain reaction (RT-qPCR)

M2 macrophages ($1x10^7$ cells/100 mm^2 petri dish) or BMDCs were treated with polypeptides (4 μg/mL), LPS (100 ng/mL), cGAMP (1 μg/mL with 10 μg/mL polyethyleneimine), or tunicamycin (10 μg/mL) for 6 h. For detection of M1- and M2-associated markers, M2 macrophages were incubated under the same treatment conditions as described above for 24 h. RNA samples were prepared according to the manufacturer's guidelines (PureLink RNA Mini Kit, ThermoFisher Scientific, USA). Briefly, 1 μg of total RNA was reverse-transcribed into complementary DNA (High Capacity cDNA Reverse Transcription Kit, ThermoFisher Scientific, USA). RT-qPCR was performed with a TaqMan™ Fast Advanced PCR master Mix (ThermoFisher Scientific, USA) with the corresponding primer (7500 FAST Real-time PCR System, Applied Biosystems, USA). Each ΔCt value was obtained by $Ct_{target} - Ct_{GAPDH}$. Each – ΔΔCt was calculated by $\Delta Ct_{cont} - \Delta Ct_{target}$. All relative mRNA levels were quantified by $2^{-\Delta\Delta Ct}$.

Phagocytosis assay

Phagocytosis was assessed by co-culturing eFluor 450-labeled cancer cells (eBioscience, USA) and carboxyfluorescein succinimidyl ester-labeled M2 macrophages (ThermoFisher Scientific, USA) or BMDCs as follows. Cancer cells (1.5×10^5 cells/12-well plate) were plated and allowed to adhere for 1 day. Then macrophages or BMDCs (4.5×10^5 cells) were added and co-cultured with the cancer cells for 1 day under the various treatment conditions. The cells were then isolated and stained with Sytox Red to exclude dead cells. The degree of phagocytosis (%) was evaluated by flow cytometry.

Antigen-presentation assay

EO771-cOVA cells were prepared as described previously.[40] M2 BMDMs or BMDCs were co-cultured with EO771-cOVA cells and treated with P1 or LPS for 24 h. Cells were stained with the corresponding antibodies and Sytox Red to exclude dead cells. The mean

fluorescence intensity of SIINFEKL-H2Kb on the M2 BMDMs was evaluated by flow cytometry.

Confocal laser scanning microscopy for phagocytosis and antigen presentation

To visualize phagocytosis, cancer cells pre-stained with eFluor 670 were seeded on confocal chamber slides (4 Chamber Slide Systems, Lab-Tek II, USA), and then M2 macrophages stained with carboxyfluorescein succinimidyl ester (CSFE) were added to the chamber with polypeptides. The cells were incubated for 6 h and then fixed with 4% para-formaldehyde solution. For antigen presentation, EO771-cOVA cells pre-seeded on the chamber were co-cultured with M2 BMDMs, and the cells were then treated with polypeptides or LPS for 1 day. The cells were fixed and then incubated with anti-SIINFEKL-H2Kb (Biolegend, USA) for another day. The chamber slides were mounted, and the cell images were obtained by confocal microscopy (FV3000, Olympus, Japan).

Western blotting

M2 BMDMs ($1.0x10^7$ cells/100 mm^2 petri dish), BMDCs ($5x10^6$ cells/6 well plate), or cancer cells (2×10^6 cells/6-well plate) were treated with experimental solutions. Each protein was extracted by using RIPA buffer containing 1% protease inhibitor and 1% phosphatase inhibitor cocktail. Protein concentrations were adjusted to 3 mg/mL by using a BCA kit, with FBS used as a standard. Electrophoresis was carried out by loading proteins (40 μg) into each lane of a sodium dodecyl sulfate-polyacrylamide gel (SDS-PAGE) gel, after which the proteins were transferred to a polyvinylidene fluoride membrane. After blocking, the polyvinylidene fluoride membrane was treated with the corresponding primary antibody, and then washed with TBS-T three times before treatment with the secondary antibody. The blot signals were visualized with a ChemiDoc MP imaging system (BioRad, USA).

Mitochondrial ROS levels

M2 macrophages (5×10^5 cells/12-well plate) or BMDCs (5×10^5 cells/12-well plate) were treated with the polypeptides, LPS, or cGAMP for 1 day before adding MitoSOX Red (2.5 μM final concentration, ThermoFisher Scientific, USA) for 10 min. The cells were rinsed with PBS three times, collected with a scraper, and stained with antibodies and cell viability dye to measure mitochondrial ROS level by flow cytometry.

mtDNA release assay

M2 macrophages (1.5×10^7 cells/100 mm^3 dish) or BMDCs (3×10^6 cells/6-well plates) were treated with polypeptides, LPS, or cGAMP for 1 day. The cytosol fraction was obtained with a Mitochondrial/Cytosol Fractionation Kit (abcam, UK) before DNA was isolated with a DNeasy Blood & Tissue Kit (QIAGEN, USA). RT-qPCR was used to measure cytosolic mtDNA contents. The copy number of cytosolic mtDNA encoding ND-1 was normalized to that of total mtDNA. For extracellular mtDNA measurement, each supernatant was collected 1 day after the treatments and then concentrated in an Amicon UltraCentifugal filter tube (MWCO:10000 g/mol, Millipore, USA). DNA isolation and mtDNA measurement were carried out as described above.

Enzyme-linked immunosorbent assay for cytokines

For supernatant collection *in vitro,* cancer cells were co-cultured with M2 BMDMs or BMDCs under different treatment conditions for 1 day. Cytokines or protein molecules (TNF-α, IL-1β, IL-2, IFN-γ, HMGB1) were quantified with mouse ELISA kits according to the manufacturer's procedures.

T-cell activation and proliferation

T cells were harvested from the spleens of OT-I or OT-II transgenic mice and isolated per the manufacturer's guidelines (EasySep Mouse T cell Isolation Kit, STEMCELL Technologies, USA). M2 macrophages or BMDCs co-cultured with cancer cells were treated with P1 or LPS for 1 day before the addition of CSFE-stained OT-I cells or OT-II cells. The cells were incubated for 3 days to allow T-cell proliferation and activation. The cells were isolated and then stained with fluorophore-tagged antibodies and cell viability dye. Flow cytometry was used to evaluate naive T cells ($CD44^{-}CD62L^{+}$), effector T cells ($CD44^{+}CD62L^{-}$) and memory T cells ($CD44^{+}CD62L^{+}$). The Invitrogen CellTrace CFSE kit was used to monitor distinct generations of proliferating cells by dye dilution.

Mice

Six- to ten-week-old C57BL/6 mice (bred at MD Anderson Cancer Center), Balb/C mice (The Jackson Laboratory, USA), *B6.129P2(SJL)-Myd88*$^{tm1.1Defr}$*/J* mice (The Jackson Laboratory, USA), *B6(C)-Cgas*$^{tm1d(EUCOMM)Hmgu}$*/J* mice (The Jackson Laboratory, USA), C57BL/6-*Tlr9*$^{em1.1Ldm}$/J mice (The Jackson Laboratory, USA), *C57BL/6J-Sting1*^{gt}*/J* mice (The Jackson Laboratory, USA), and B6.FVB-*1700016L21Rik*$^{Tg(Itgax-DTR/EGFP)57Lan}$*/J* mice (The Jackson Laboratory, USA) were maintained at the animal facility of The University of Texas MD Anderson Cancer Center in specific-pathogen-free environments. All animal use was approved by the Institutional Animal Care and Use Committee of MD Anderson Cancer Center, and all experiments complied with approved protocols and institutional policies.

Pharmacokinetics and biodistribution

Before being studied, P1, P2, and P3 were labeled with IR800CW-NHS ester (LICOR, USA) and conjugated according to the manufacturer's protocol. Briefly, IR800CW-tagged P1, P2, or P3 (10 mg/kg) were intravenously injected into EO771-tumor bearing mice. For pharmacokinetic studies, blood was collected via cardiac puncture at predetermined timepoints (0.5, 1, 2, 4, 8, 12, and 24 h). All blood samples were transferred to a black 96-well plate, and images obtained with the *in vivo* imaging system (IVIS) were photographed to measure the polypeptide concentration in blood plasma (λ_{ex}=789 nm, λ_{em}=814 nm). Each fluorescence intensity was converted to polypeptide concentration based on the standard curve. ID% in blood plasma was calculated by $F_{\text{sample}}/F_{\text{initial dose}}$. For biodistribution studies, IVIS images were taken at the same times as described above. The mice were killed, and organs harvested at 24 h after the polypeptide injection, and then the IVIS was used to image the excised organs (liver, kidney, lung, heart, spleen, and tumor) to quantify the fluorescence signals. For visualization of FITC-tagged P1, P2, and P3 via confocal laser scanning microscopy, tumor tissues obtained 24 h after the

treatments were fixed with 4% paraformaldehyde, cryo-embedded with optimal cutting temperature compound, and cryo-sectioned in 5-μm sections. Tumor sections were incubated with primary F4/80 antibody overnight and then stained with fluorophore-labeled secondary antibodies for 2 h. Nuclei were stained with 4',6-diamidino-2-phenylindole (DAPI; 1 μg/mL, Milipore Merck, USA), and immunohistologic images were obtained by confocal laser scanning microscopy.

Tumor models

Orthotopic breast tumor models were established by implanting EO771 (1.5×10^6 cells) or 4T1 (5×10^5 cells) breast cancer cells into a mammary pad in mice. Tumors were measured with calipers, and tumor volumes were calculated as ellipsoids ($\pi/6 \times \text{length} \times \text{width}^2$). Mice with tumors of similar size were randomly sorted into experimental groups on day 10 after tumor-cell inoculation. Treatments (P1, P2, P3, cGAMP, CpG, ADU-S100, MSA2: 10 mg/kg for EO771 tumor; P1 20 mg/kg for 4T1 tumor; intravenous injection) took place on days 10, 12, and 14 for EO771 tumors, and on days 8, 10, and 12 for 4T1 tumors. For combined therapy, αPD1 (200 μg, intraperitoneal injection, BioXcell, USA) was given on days 11, 13, and 15 for either EO771 or 4T1 tumors. For antitumor evaluation of the large (EO771) tumors, treatments were given when the EO771 tumor volume exceeded 100 mm^3. Mice were euthanized with CO_2 if tumor volumes exceeded 1000 mm^3 or ulcerations (>5 mm in diameter) developed.

Flow cytometry *in vivo*

Tumors and spleens were excised from tumor-bearing mice 1 or 2 days after the final treatment. Tumors were dissociated into single-cell suspensions by using a mouse Tumor Dissociation Kit (Miltenyi Biotech). $CD45^+$ cells were enriched by using a CD45-positive selection method (CD45 Microbeads mouse, Miltenyi Biotech, USA). Splenocytes were obtained by grinding the spleens and then lysing red blood cells. Both types of cells were stained with the corresponding antibodies for analysis by flow cytometry.

Immunohistochemical assays

Tumor tissues were excised 1 or 2 days after the final treatment, fixed with 4% paraformaldehyde, embedded in paraffin, and sliced into 5-μm sections. Tumor sections were then deparaffinized and stained with the corresponding primary antibodies, incubated overnight, and then stained with fluorophore-labeled secondary antibodies for 1 h. Nuclei were stained with DAPI (1 μg/mL, Milipore Merck, USA), and immunohistologic images were obtained by confocal laser scanning microscopy.

OVA tetramer assay

EO771-cOVA cells (1.5×10^6) were inoculated into the mammary pad of C57/BL6 mice. Treatments with HEPES, P1, αPD1, P1+αPD1, or cGAMP+αPD1 were given intravenously to tumor-bearing mice from day 10 to day 15. Tumors harvested on day 17 were dissociated, and tumor-infiltrating lymphocytes were isolated by the $CD45^+$ enrichment method described above. Cells were stained with Fixable far red cell viability

dye, PE antiCD3, BV650 antiCD8, or BV421 OVA tetramer (MBL, USA) to verify OVA tetramer$^+$CD3$^+$CD8$^+$ populations.

RT-qPCR *in vivo*

Tumors excised 1 day after the final treatment were dissociated into single-cell suspensions by using a mouse Tumor Dissociation Kit (Miltenyi Biotech, USA). F4/80$^+$ cells (for macrophages) and CD11c$^+$ cells (for DCs) were isolated by using F4/80 and CD11c magnetic beads (Miltenyi Biotech, USA), respectively. RNAs from tumor-infiltrating APCs were extracted according to the manufacturer's guidelines with a PureLink RNA Mini Kit (ThermoFisher Scientific, USA). RT-qPCR was conducted as described earlier.

Macrophage depletion assay

C57/BL6 mice were injected intraperitoneally with anti-CSF1R mAbs (300 μg, BioXcell, USA) every 3 days beginning 2 days before the treatments. Macrophage depletion was confirmed by flow cytometry of CD45$^+$ cells isolated from the EO771 tumor tissues of the mice or by immunofluorescence of F4/80 in tumor tissue sections.

DC depletion assay

CD11c-DTR/GFP mice (>8 weeks old) were injected intraperitoneally with diphtheria toxin (100 ng, Corning, USA) every 3 days beginning 2 days before the treatments. CD11c depletion was verified by flow cytometry of CD45$^+$ cells isolated from the EO771 tumor tissue of the mice or by immunofluorescence of CD11c in tumor tissue sections.

CD8$^+$ T-cell depletion assay

C57/BL6 mice were injected intraperitoneally with anti-CD8α mAbs (300 μg, BioXcell, USA) every 4 days beginning 3 days before the various treatments. CD8$^+$ T-cell depletion was confirmed by flow cytometry of CD8$^+$ T cells isolated from the spleens of the mice.

Tumor metastasis model

The spontaneous metastatic breast tumor model was established by injecting 4T1-BR4-mcherry Luc cells (1.5×10^6 cells or 1×10^6 cells for the rechallenge study) into the mammary pad, and the resulting tumors were resected 14 days later. Treatments were implemented on day 16, 18, and 20 for P1 and cGAMP (20 mg/kg, intravenous injection) or day 17, 19, and 21 for αPD1 (200 μg, intraperitoneal injection). Spontaneous 4T1 metastases were visualized with an IVIS spectrum imaging system (IVIS Lumina XR, Perkin Elmer). For the rechallenge experiment, 4T1-BR4-mcherry Luc cells (1.0×10^6 cells) were inoculated into the mammary pad, and the established tumors were resected on day 12 before treatments were given on day 14, 16 and 18 for HEPES or P1 (20 mg/kg, intravenous) or day 15, 17 and 19 for αPD1 (200 μg, intraperitoneal). Mouse survival was monitored until day 60 after tumor inoculation, and naïve and immunized mice (with long-term survival) were re-implanted with 4T1-BR4-mcherry Luc cells (1.0×10^6 cells). Tumor volumes were measured after day 5 after tumor re-inoculation every other day.

Statistical analysis

All data are shown as means and standard deviation (SD) from at least triplicate conditions unless otherwise indicated. Statistical analyses involved unpaired Student's *t* test for two groups or one-way analysis of variance (ANOVA) for multiple comparisons. Survival was assessed by the Kaplan-Meier method and compared by the log-rank (Mantel-Cox) test. *P* values of <0.05 were regarded as indicating statistically significant differences. Statistical analyses were conducted with Graph Prism 9 for ordinary one-way ANOVA or log-rank test and Microsoft Excel 2020 for unpaired Student's *t* test. No animals were excluded from the analyses. Quantitative analyses of confocal laser scanning microscopy images were carried out with ImageJ.

Extended Data

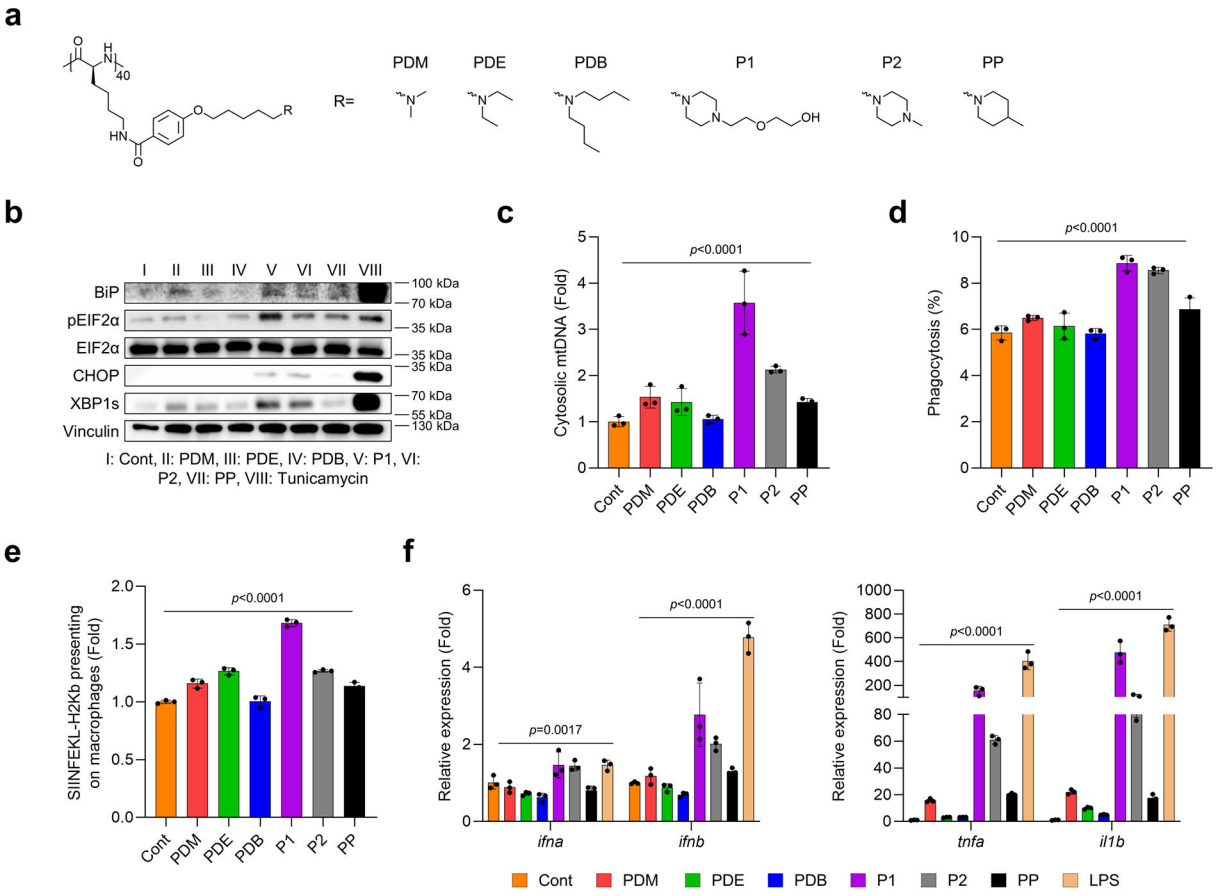

Extended Fig. 1. Varying hydrophobicity in the engineered polypeptide affects immunogenicity via ER stress-mediated mtDNA release and effector functions in macrophages.

(a) Chemical structure of cationic polypeptides with different amine-containing analogues. Cationic polypeptides including hydrophilic analogues and cyclic structures more favorably induced (b) ER stress and (c) mtDNA release in bone marrow-derived macrophages (BMDMs) [n=3, mean±standard deviation (SD)], ordinary one-way analysis of variance (ANOVA). Cationic polypeptide tethered with a hydrophilic building block and cyclic structure increased (d) phagocytosis of EO771 breast cancer cells and (e) cross-presentation

of the model antigen SIINFEKL-H2Kb (n=3, mean±SD), ordinary one-way ANOVA. (f) Gene expression of pro-inflammatory cytokines was affected by hydrophobicity of polypeptides and the chemical structure of amine-including analogues (n=3, mean±SD), ordinary one-way ANOVA.

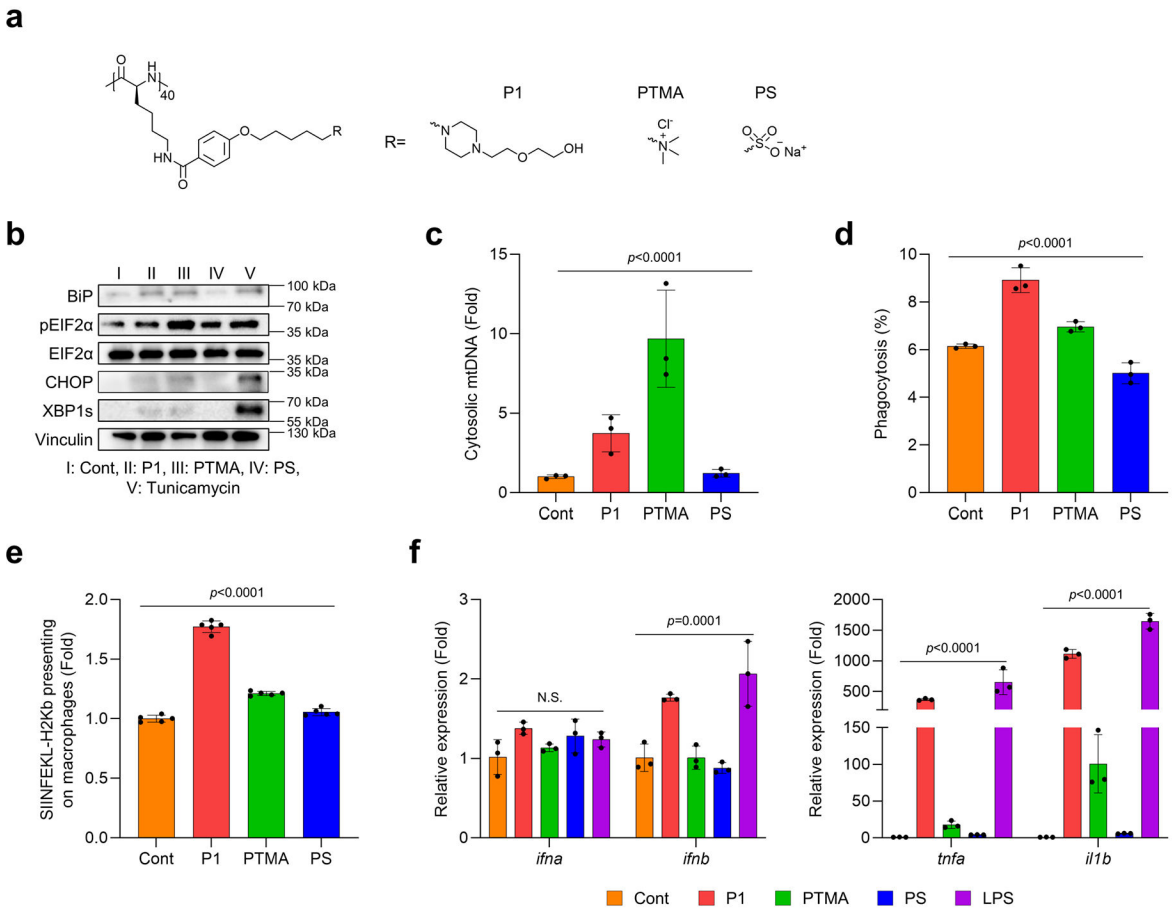

Extended Fig. 2. Varying the electrostatic charge of the polypeptide affects immunogenicity via ER stress-mediated mtDNA release and effector functions in macrophages.

(a) Chemical structure of polypeptides with different electrolytes. P1 more favorably induced (b) ER stress and (c) mtDNA release in BMDMs greater than did PTMA (strongly cationic) and PS (anionic) (n=3, mean±SD), ordinary one-way ANOVA. P1 improved (d) phagocytosis of EO771 breast cancer cells and (e) cross-presentation of the model antigen SIINFEKL-H2Kb to a greater extent than did PTMA or PS (n=3, mean±SD), ordinary one-way ANOVA. (f) Expression of genes for pro-inflammatory cytokines was regulated by types of electrolytes and strength of cationic charges (n=3, mean±SD), ordinary one-way ANOVA.

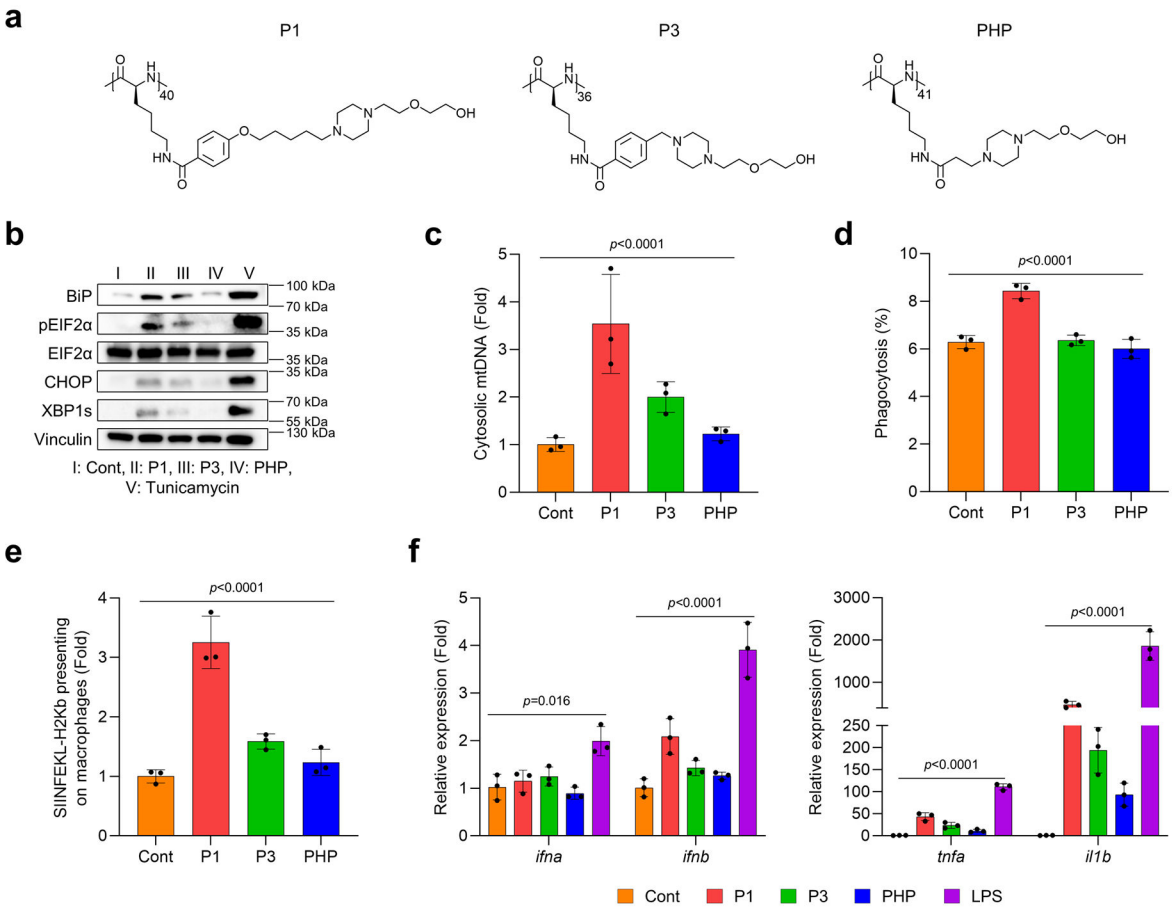

Extended Fig. 3. Varying the length of the side chain of the polypeptide regulates immunogenicity via ER stress-mediated mtDNA release and effector functions in macrophages.

(a) Chemical structures of polypeptides with side chains of different lengths. P1 induced (b) ER stress and (c) mtDNA release in BMDMs more strongly than did P3 (mid-length) and PS (short length) (n=3, mean±SD), ordinary one-way ANOVA. P1 improved (d) phagocytosis of EO771 breast cancer cells and (e) cross-presentation of the model antigen SIINFEKL-H2Kb to a greater extent than did P3 and P1 (n=3, mean±SD), ordinary one-way ANOVA. (f) Expression of genes for pro-inflammatory cytokines was affected by the length of side chains in the polypeptides (n=3, mean±SD), ordinary one-way ANOVA.

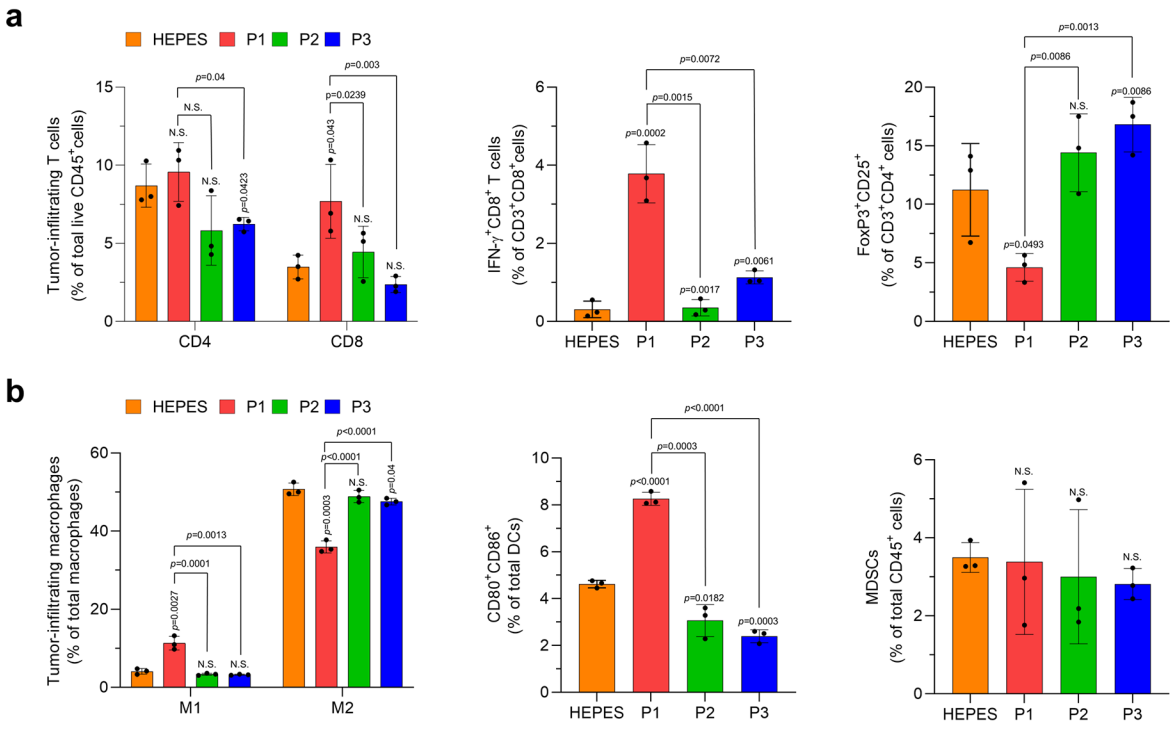

Extended Fig. 4. P1 promotes innate and adaptive immune activation within the tumor microenvironment.

(a) P1 increased the population of tumor-infiltrating $CD8^+$ T cells and IFNγ-producing $CD8^+$ T cells, but decreased that of Tregs ($CD3^+CD4^+CD25^+FoxP3^+$), relative to P2 and P3 (n=3, mean±SD). Tumor-infiltrating lymphocytes were obtained on day 16 (2 days after the last treatment). (b) P1 promoted M1 macrophage polarization (M1 macrophage: $CD206^-CD80^+CD86^+$; M2 macrophage: $CD206^+CD80^-$; macrophages: $CD11b^+CD11c^-F4/80^+MHC\text{-}II^-$) and maturation of dendritic cells (DCs) (Mature DCs: $CD80^+CD86^+$ DC; DC: $CD11c^+MHC\text{-}II^+F4/80^-$) but did not affect the number of myeloid-derived suppressor cells (MDSCs) ($CD11b^+CD11c^-MHC\text{-}II^-F4/80^-Gr\text{-}1^+$) within the tumor microenvironment relative to P2 and P3 (n=3, mean±SD), unpaired Student's *t* test in comparison with Cont and the indicated conditions.

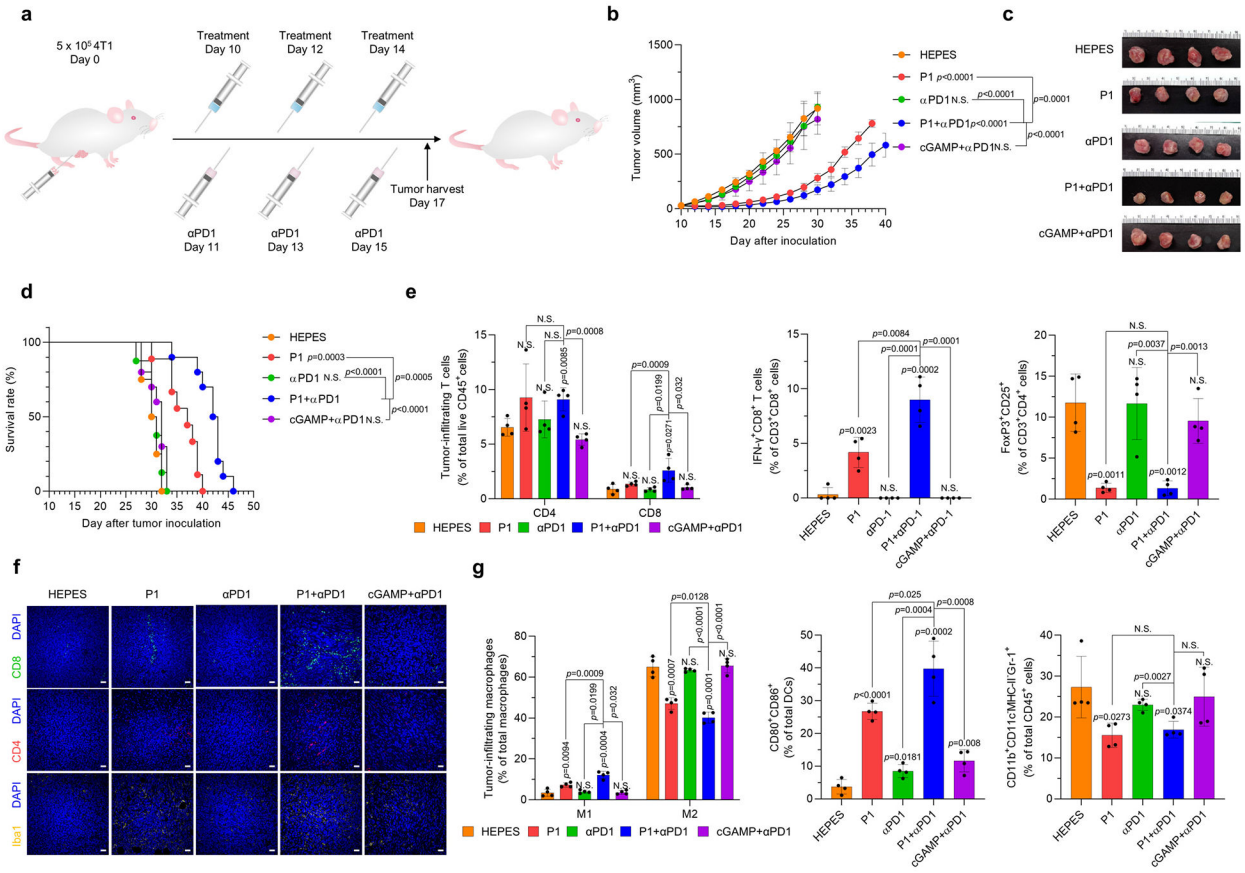

Extended Fig. 5. P1 combined with αPD1 evoked strong antitumor immunity in mice bearing metastatic tumors.

(a) Timeline for tumor establishment and administration of P1 and αPD1. (b) Growth curves for 4T1 tumors in mice after the indicated treatments (n=8 for HEPES; n=9 for P1; n=10 for P1+αPD1 and cGAMP+αPD1; mean±SD), unpaired Student's *t* test in comparison with HEPES or the indicated conditions on day 30 after tumor inoculation. (c) Photographs of excised 4T1 tumor tissues on day 17. (d) Kaplan-Meier survival curves of 4T1 tumor-bearing mice; log-rank (Mantel-Cox) test in comparison with HEPES or the indicated conditions. (e) Flow cytometry of tumor-infiltrating T lymphocytes (Tregs: $CD3^+CD4^+CD25^+FoxP3^+$) and their subsets (n=4, mean±SD), which were harvested on day 17. (f) Immunofluorescence stains for CD4, CD8, and Iba1 in macrophages (scale bar, 30 μm). (g) Profiles of tumor-infiltrating myeloid cells (M1 macrophage: $CD206^-CD80^+CD86^+$; M2 macrophage: $CD206^+CD80^-$; macrophage: $CD11b^+CD11c^-F4/80^+MHC\text{-}II$; mature DC: $CD80^+CD86^+$ DC; DC: $CD11c^+MHC\text{-}II^+F4/80^-$; MDSC: $CD11b^+CD11c^-MHC\text{-}II^-F4/80^-Gr\text{-}1^+$) as evaluated by flow cytometry (n=4, mean±SD); unpaired Student's *t* test in comparison with Cont or the indicated condition.

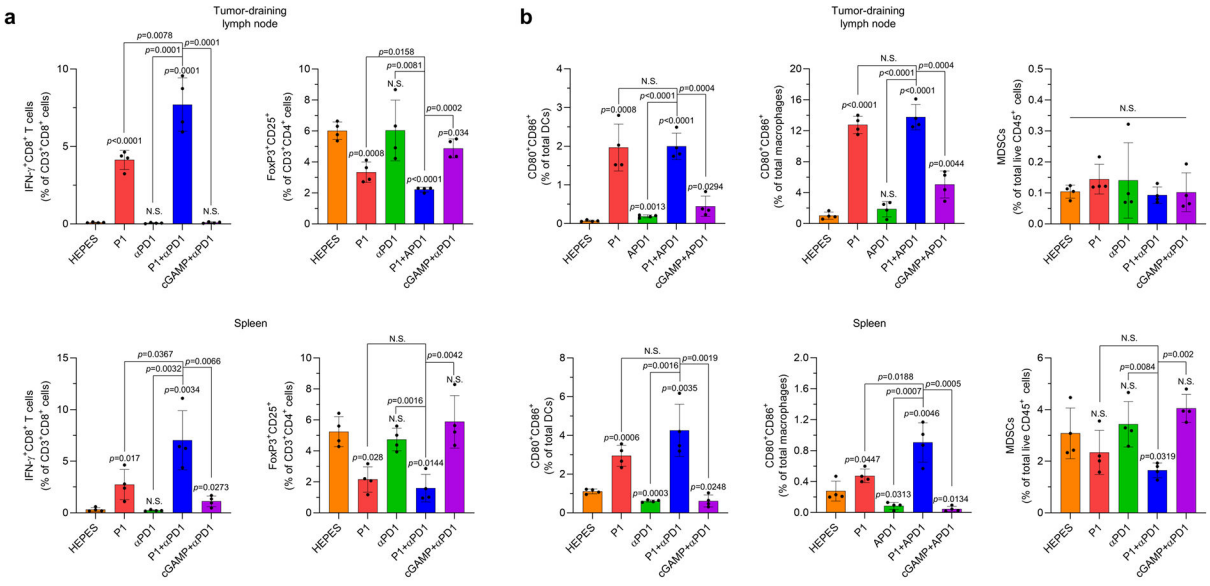

Extended Fig. 6. P1 combined with αPD1 generates robust systemic antitumor immunity.

(a) P1+αPD1 treatment increased the production of IFNγ from $CD8^+$ T cells and decreased the population of Tregs ($CD3^+CD4^+CD25^+FoxP3^+$) in tumor-draining lymph nodes and spleen as compared with the other treatment conditions (n=4, mean±SD), unpaired Student's *t* test in comparison with HEPES or the indicated conditions. (b) P1+αPD1 treatment increased the population of mature DCs ($CD11c^+F4/80^-MHC\text{-}II^+CD80^+CD86^+$) and pro-inflammatory macrophages polarization ($CD80^+CD86^+CD11b^+CD11c^-F4/80^+$ for migratory macrophages in spleen, $CD80^+CD86^+CD11b^+CD11c^-F4/80^+$ for macrophages in lymph nodes), but maintained the numbers of MDSCs ($CD11b^+CD11c^-F4/80^-MHC\text{-}II^-Gr\text{-}1^+$) in tumor-draining lymph nodes and spleen, relative to the other treatments (n=4, mean±SD); unpaired Student's *t* test in comparison with HEPES or the indicated conditions.

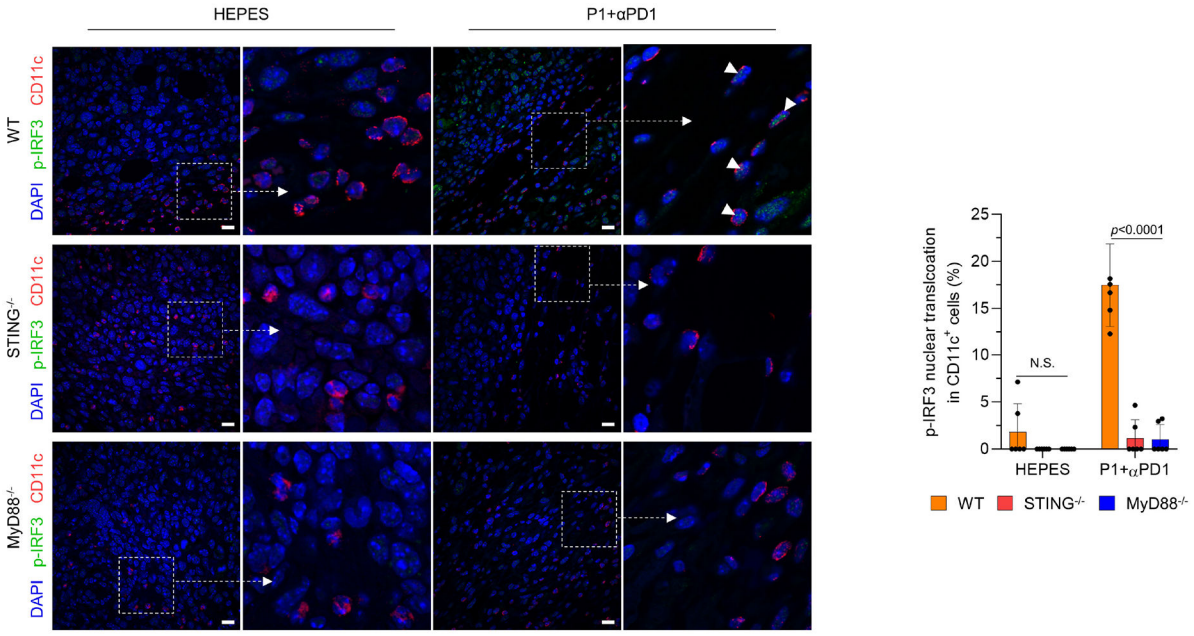

Extended Fig. 7. Activation of MyD88 and STING is required to stimulate the p-IRF3 axis in tumor-homing dendritic cells (DCs) treated with P1+αPD1.

Immunofluorescence images show that DCs treated with P1+αPD1 promoted p-IRF3 nuclear translocation (white arrows) in WT but not in STING$^{-/-}$ or MyD88$^{-/-}$ cells. Scale bar, 30 μm. Numbers of nucleus-translocating p-IRF3^{+} DCs in the immunofluorescence images were counted with ImageJ software (n=6 independent images, mean±SD).

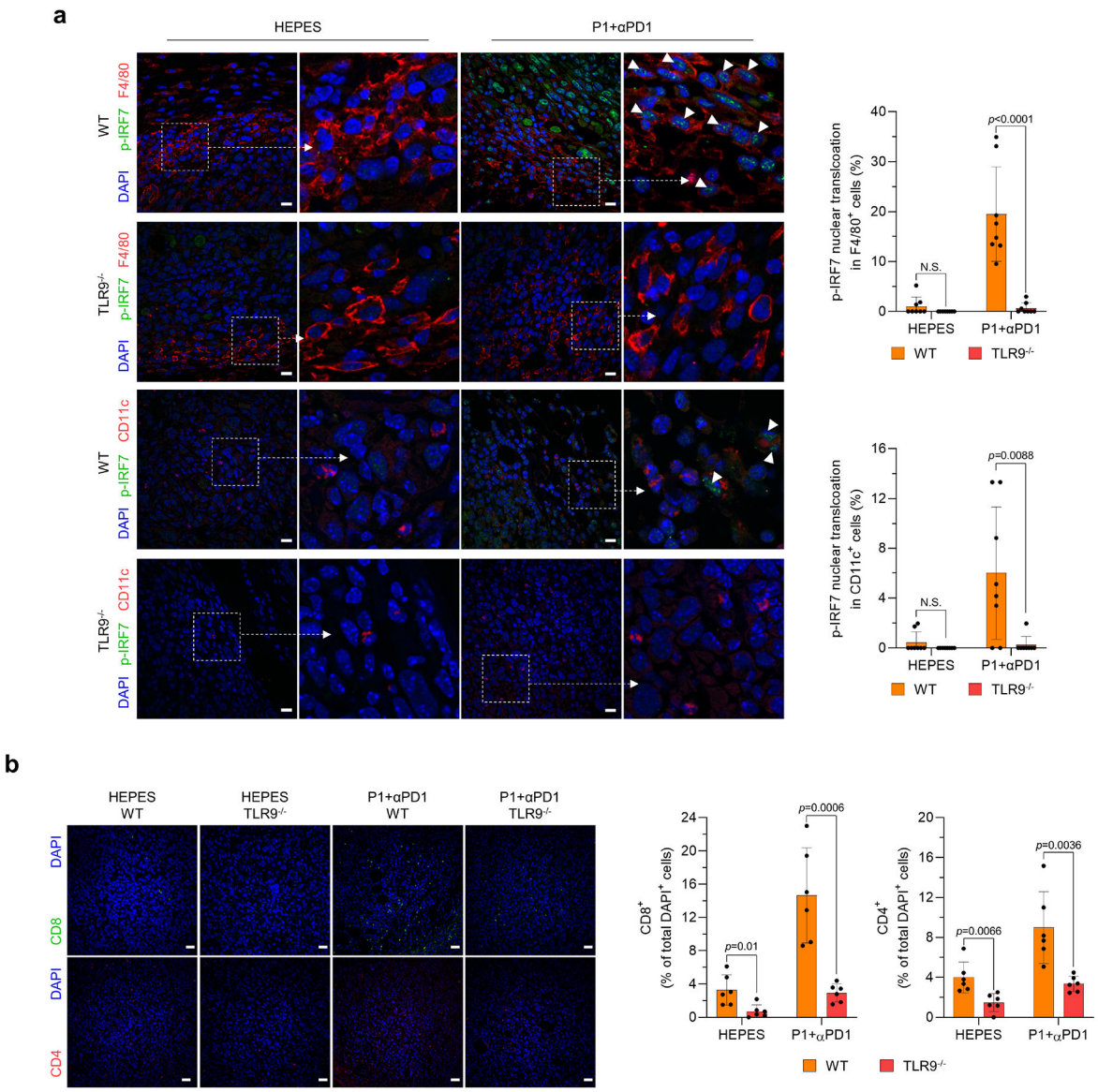

Extended Fig. 8. TLR9 activation is required to recruit tumor-infiltrating T cells by stimulating IRF7 signaling in tumor-homing APCs treated with P1+αPD1.

(a) P1+αPD1 treatment promoted p-IRF7 nuclear translocation in macrophages and DCs in WT but not in TLR9$^{-/-}$ mice; scale bar, 30 μm; unpaired Student's *t* test in comparison to the indicated conditions (n=8 independent images, mean±SD). (b) P1+αPD1 treatment of TLR9$^{-/-}$ mice blocked recruitment of both CD4^{+} and CD8^{+} T cells into tumors; scale bar, 20 μm; unpaired Student's *t* test in comparison to the indicated conditions (n=6 independent images, mean±SD). Numbers of cells in the immunofluorescence images were counted by ImageJ software.

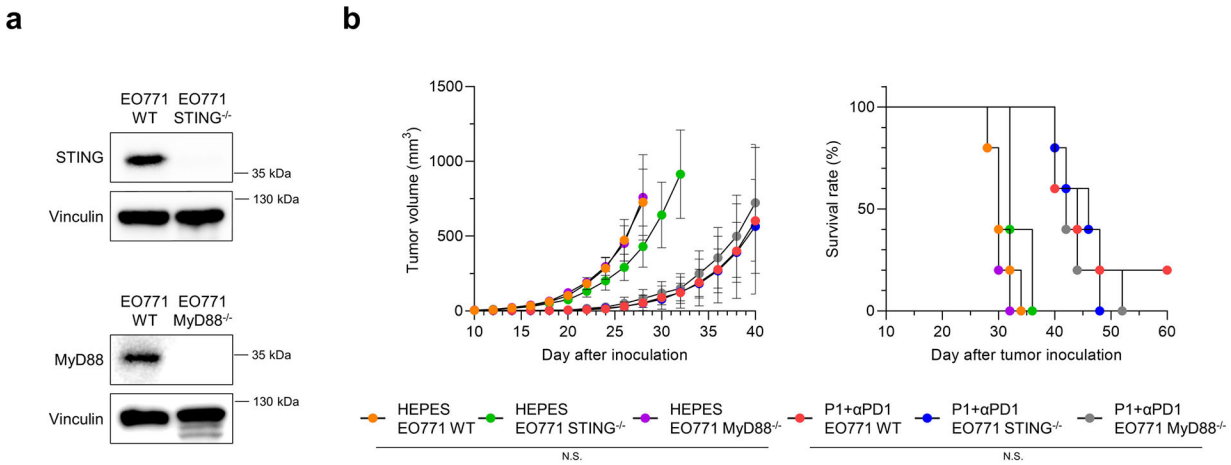

Extended Fig. 9. Activation of STING and MyD88 in cancer cells is not required for P1+αPD1's antitumor effect.

(a) Immunoblots verifying that EO771 STING$^{-/-}$ cells did not express STING, and EO771 MyD88$^{-/-}$ cells did not express MyD88. (b) Tumor growth curves for mice with EO771 WT, EO771 STING$^{-/-}$, or EO771 MyD88$^{-/-}$ tumors after intravenous injection of HEPES or P1+αPD1 (n=5, mean±SD). (c) Kaplan-Meier survival curves for mice with EO771 WT, EO771 STING$^{-/-}$, or EO771 MyD88$^{-/-}$ tumors; log-rank (Mantel-Cox) test compared with the indicated conditions.

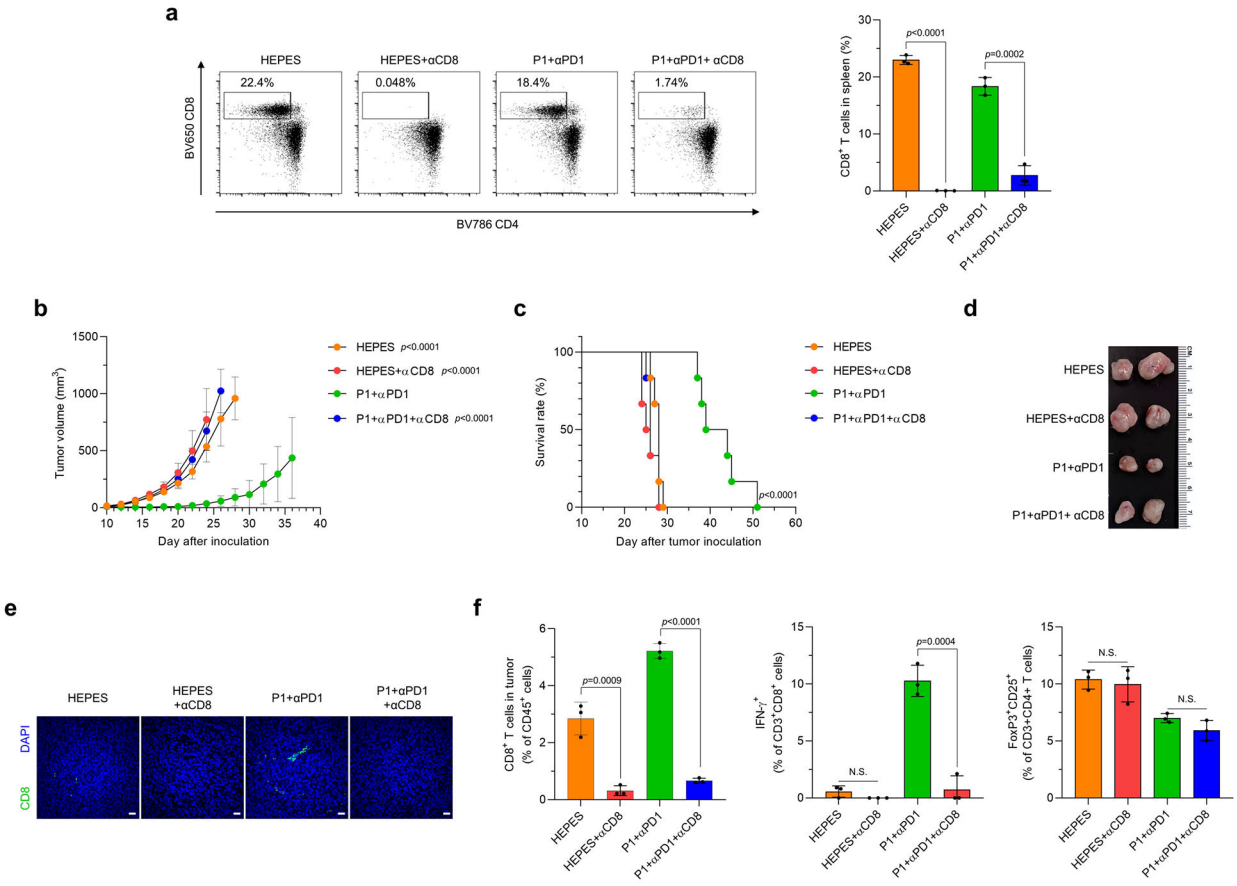

Extended Fig. 10. CD8$^+$ T-cell depletion abolished adaptive immunity conferred by P1+αPD1.

(a) CD8$^+$ T cell populations in splenocytes, evaluated by flow cytometry on day 17 after tumor cell inoculation (n=3, mean±SD). (b,c) CD8 depletion (b) abrogated the antitumor effect of P1+αPD1 and (c) reduced the survival of EO771 tumor-bearing mice (n=6, mean±SD); unpaired Student's *t* test in comparison to P1+αPD1 at day 24 after tumor inoculation for tumor growth curve; log-rank (Mantel-Cox) test for Kaplan-Meier survival curve. (d) Excised tumors from each experimental group show that CD8 depletion eliminated the antitumor effect of P1+αPD1. (e) Immunofluorescence stains of tumor-infiltrating CD8$^+$ T cells show that CD8 depletion inhibited the recruitment of CD8$^+$ T cells within tumors; scale bar, 30 μm. (f) CD8 depletion reduced the proportions of tumor-infiltrating CD8$^+$ T cells and IFN-γ$^+$CD8$^+$ T cells, but did not change the proportion of Tregs (n=3, mean±SD); Unpaired Student's *t* test; n.s., not significant compared with the indicated conditions.

Supplementary Material

Refer to Web version on PubMed Central for supplementary material.

Acknowledgements

Supported in part by the National Cancer Institute Grant 1K08 CA241070 to W.J.; US Department of Defense grant W81XWH-19-1-0325 to B.Y.S.K., and the Cancer Center Support (Core) Grant P30 CA016672 from the National

Cancer Institute, National Institutes of Health, to The University of Texas MD Anderson Cancer Center (PI: PW Pisters). The authors thank Christine Wogan of the Division of Radiation Oncology, MD Anderson Cancer Center, for editorial assistance.

References

1. von Roemeling CA et al. Therapeutic modulation of phagocytosis in glioblastoma can activate both innate and adaptive antitumour immunity. Nature Communications 11, 1508, doi:10.1038/s41467-020-15129-8 (2020).
2. Lee D, Huntoon K, Wang Y, Jiang W & Kim BYS Harnessing Innate Immunity Using Biomaterials for Cancer Immunotherapy. Advanced Materials 33, 2007576, doi:10.1002/adma.202007576 (2021).
3. Lu Y et al. Immunological conversion of solid tumours using a bispecific nanobioconjugate for cancer immunotherapy. Nature Nanotechnology 17, 1332–1341, doi:10.1038/s41565-022-01245-7 (2022).
4. Nagarsheth N, Wicha MS & Zou W Chemokines in the cancer microenvironment and their relevance in cancer immunotherapy. Nature Reviews Immunology 17, 559–572, doi:10.1038/nri.2017.49 (2017).
5. Binnewies M et al. Understanding the tumor immune microenvironment (TIME) for effective therapy. Nature Medicine 24, 541–550, doi:10.1038/s41591-018-0014-x (2018).
6. Lee D et al. Harnessing cGAS-STING Pathway for Cancer Immunotherapy: From Bench to Clinic. Advanced Therapeutics n/a, 2200040, doi:10.1002/adtp.202200040 (2022).
7. Riley JS & Tait SWG Mitochondrial DNA in inflammation and immunity. EMBO reports 21, e49799, doi:10.15252/embr.201949799 (2020). [PubMed: 32202065]
8. Ramanjulu JM et al. Design of amidobenzimidazole STING receptor agonists with systemic activity. Nature 564, 439–443, doi:10.1038/s41586-018-0705-y (2018). [PubMed: 30405246]
9. Pan B-S et al. An orally available non-nucleotide STING agonist with antitumor activity. Science 369, eaba6098, doi:10.1126/science.aba6098 (2020). [PubMed: 32820094]
10. Chin EN et al. Antitumor activity of a systemic STING-activating non-nucleotide cGAMP mimetic. Science 369, 993–999, doi:10.1126/science.abb4255 (2020). [PubMed: 32820126]
11. Wu Y.-t. et al. Tumor-targeted delivery of a STING agonist improves cancer immunotherapy. Proceedings of the National Academy of Sciences 119, e2214278119, doi:10.1073/pnas.2214278119 (2022).
12. Sun X et al. Amplifying STING activation by cyclic dinucleotide–manganese particles for local and systemic cancer metalloimmunotherapy. Nature Nanotechnology 16, 1260–1270, doi:10.1038/s41565-021-00962-9 (2021).
13. Dane EL et al. STING agonist delivery by tumour-penetrating PEG-lipid nanodiscs primes robust anticancer immunity. Nature Materials 21, 710–720, doi:10.1038/s41563-022-01251-z (2022). [PubMed: 35606429]
14. Radovic-Moreno AF et al. Immunomodulatory spherical nucleic acids. Proceedings of the National Academy of Sciences 112, 3892–3897, doi:10.1073/pnas.1502850112 (2015).
15. Li X et al. Cancer immunotherapy based on image-guided STING activation by nucleotide nanocomplex-decorated ultrasound microbubbles. Nature Nanotechnology 17, 891–899, doi:10.1038/s41565-022-01134-z (2022).
16. Luo M et al. A STING-activating nanovaccine for cancer immunotherapy. Nature Nanotechnology 12, 648–654, doi:10.1038/nnano.2017.52 (2017).
17. Li S et al. Prolonged activation of innate immune pathways by a polyvalent STING agonist. Nature Biomedical Engineering 5, 455–466, doi:10.1038/s41551-020-00675-9 (2021).
18. Miao L et al. Delivery of mRNA vaccines with heterocyclic lipids increases anti-tumor efficacy by STING-mediated immune cell activation. Nature Biotechnology 37, 1174–1185, doi:10.1038/s41587-019-0247-3 (2019).
19. Lee D, Huntoon K, Lux J, Kim BYS & Jiang W Engineering nanomaterial physical characteristics for cancer immunotherapy. Nature Reviews Bioengineering, doi:10.1038/s44222-023-00047-3 (2023).

20. Wang J et al. Physical activation of innate immunity by spiky particles. Nature Nanotechnology 13, 1078–1086, doi:10.1038/s41565-018-0274-0 (2018).
21. Leigh T & Fernandez-Trillo P Helical polymers for biological and medical applications. Nature Reviews Chemistry 4, 291–310, doi:10.1038/s41570-020-0180-5 (2020). [PubMed: 37127955]
22. Song Z et al. Secondary structures in synthetic polypeptides from N-carboxyanhydrides: design, modulation, association, and material applications. Chemical Society Reviews 47, 7401–7425, doi:10.1039/C8CS00095F (2018). [PubMed: 30175827]
23. Song Z et al. Synthetic polypeptides: from polymer design to supramolecular assembly and biomedical application. Chemical Society Reviews 46, 6570–6599, doi:10.1039/C7CS00460E (2017). [PubMed: 28944387]
24. Fang Y et al. MAL2 drives immune evasion in breast cancer by suppressing tumor antigen presentation. The Journal of Clinical Investigation 131, doi:10.1172/JCI140837 (2021).
25. Wculek SK et al. Dendritic cells in cancer immunology and immunotherapy. Nature Reviews Immunology 20, 7–24, doi:10.1038/s41577-019-0210-z (2020).
26. Anderson DA, Dutertre C-A, Ginhoux F & Murphy KM Genetic models of human and mouse dendritic cell development and function. Nature Reviews Immunology 21, 101–115, doi:10.1038/s41577-020-00413-x (2021).
27. Russell DG, Huang L & VanderVen BC Immunometabolism at the interface between macrophages and pathogens. Nature Reviews Immunology 19, 291–304, doi:10.1038/s41577-019-0124-9 (2019).
28. West AP & Shadel GS Mitochondrial DNA in innate immune responses and inflammatory pathology. Nature Reviews Immunology 17, 363–375, doi:10.1038/nri.2017.21 (2017).
29. Gay NJ, Symmons MF, Gangloff M & Bryant CE Assembly and localization of Toll-like receptor signalling complexes. Nature Reviews Immunology 14, 546–558, doi:10.1038/nri3713 (2014).
30. Swanson KV, Deng M & Ting JPY The NLRP3 inflammasome: molecular activation and regulation to therapeutics. Nature Reviews Immunology 19, 477–489, doi:10.1038/s41577-019-0165-0 (2019).
31. Gaidt MM et al. The DNA Inflammasome in Human Myeloid Cells Is Initiated by a STING-Cell Death Program Upstream of NLRP3. Cell 171, 1110–1124.e1118, doi:10.1016/j.cell.2017.09.039 (2017). [PubMed: 29033128]
32. Crouse J, Kalinke U & Oxenius A Regulation of antiviral T cell responses by type I interferons. Nature Reviews Immunology 15, 231–242, doi:10.1038/nri3806 (2015).
33. Zitvogel L, Galluzzi L, Kepp O, Smyth MJ & Kroemer G Type I interferons in anticancer immunity. Nature Reviews Immunology 15, 405–414, doi:10.1038/nri3845 (2015).
34. Honda K, Takaoka A & Taniguchi T Type I Inteferon Gene Induction by the Interferon Regulatory Factor Family of Transcription Factors. Immunity 25, 349–360, doi:10.1016/j.immuni.2006.08.009 (2006). [PubMed: 16979567]
35. Xu J et al. A general strategy towards personalized nanovaccines based on fluoropolymers for post-surgical cancer immunotherapy. Nature Nanotechnology 15, 1043–1052, doi:10.1038/s41565-020-00781-4 (2020).
36. Rolfo C, Giovannetti E, Martinez P, McCue S & Naing A Applications and clinical trial landscape using Toll-like receptor agonists to reduce the toll of cancer. npj Precision Oncology 7, 26, doi:10.1038/s41698-023-00364-1 (2023). [PubMed: 36890302]
37. Meric-Bernstam F et al. Phase Ib study of MIW815 (ADU-S100) in combination with spartalizumab (PDR001) in patients (pts) with advanced/metastatic solid tumors or lymphomas. Journal of Clinical Oncology 37, 2507–2507, doi:10.1200/JCO.2019.37.15_suppl.2507 (2019).
38. Harrington KJ et al. LBA15 - Preliminary results of the first-in-human (FIH) study of MK-1454, an agonist of stimulator of interferon genes (STING), as monotherapy or in combination with pembrolizumab (pembro) in patients with advanced solid tumors or lymphomas. Annals of Oncology 29, viii712, doi:10.1093/annonc/mdy424.015 (2018).
39. Dongye Z, Li J & Wu Y Toll-like receptor 9 agonists and combination therapies: strategies to modulate the tumour immune microenvironment for systemic anti-tumour immunity. British Journal of Cancer 127, 1584–1594, doi:10.1038/s41416-022-01876-6 (2022). [PubMed: 35902641]

40. Kim S-Y et al. Multivalent Polymer Nanocomplex Targeting Endosomal Receptor of Immune Cells for Enhanced Antitumor and Systemic Memory Response. Angewandte Chemie International Edition 54, 8139–8143, doi:10.1002/anie.201501380 (2015). [PubMed: 26014442]

41. Carroll EC et al. The Vaccine Adjuvant Chitosan Promotes Cellular Immunity via DNA Sensor cGAS-STING-Dependent Induction of Type I Interferons. Immunity 44, 597–608, doi:10.1016/j.immuni.2016.02.004 (2016). [PubMed: 26944200]

42. Jneid B et al. Selective STING stimulation in dendritic cells primes antitumor T cell responses. Science Immunology 8, eabn6612, doi:10.1126/sciimmunol.abn6612.

43. Kim JT et al. Dendritic cell–targeted lentiviral vector immunization uses pseudotransduction and DNA-mediated STING and cGAS activation. Science Immunology 2, eaal1329, doi:10.1126/sciimmunol.aal1329 (2017). [PubMed: 28733470]

44. An J et al. Enhancement of the viability of T cells electroporated with DNA via osmotic dampening of the DNA-sensing cGAS–STING pathway. Nature Biomedical Engineering, doi:10.1038/s41551-023-01073-7 (2023).

45. Jeong SD et al. Immunogenic Cell Death Inducing Fluorinated Mitochondria-Disrupting Helical Polypeptide Synergizes with PD-L1 Immune Checkpoint Blockade. Advanced Science 8, 2001308, doi:10.1002/advs.202001308 (2021). [PubMed: 33854870]

46. Lee D et al. Polypeptide-Based K+ Ionophore as a Strong Immunogenic Cell Death Inducer for Cancer Immunotherapy. ACS Applied Bio Materials 4, 8333–8342, doi:10.1021/acsabm.1c00861 (2021).

47. Lee D et al. A Helical Polypeptide-Based Potassium Ionophore Induces Endoplasmic Reticulum Stress-Mediated Apoptosis by Perturbing Ion Homeostasis. Advanced Science 6, 1801995, doi:10.1002/advs.201801995 (2019). [PubMed: 31380199]

48. Yuan H et al. Multivalent bi-specific nanobioconjugate engager for targeted cancer immunotherapy. Nature Nanotechnology 12, 763–769, doi:10.1038/nnano.2017.69 (2017).

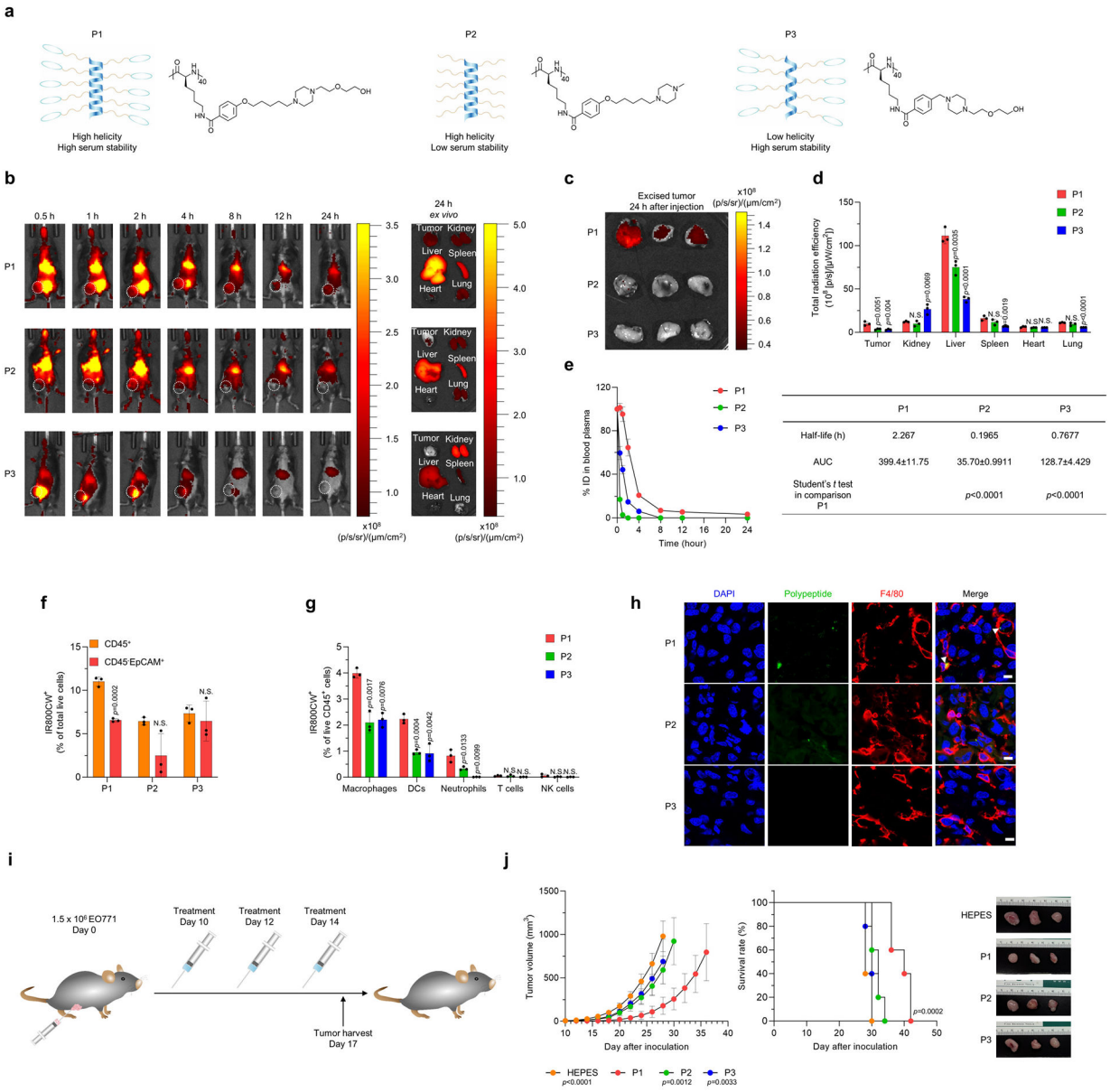

Fig. 1. Physiochemical characterization and antitumor evaluation of polypeptides *in vivo*.

(a) Schematic illustration and chemical structure of the P1, P2, and P3 polypeptides. (b) Representative fluorescence images of EO771 tumor-bearing mice taken at predetermined times after intravenous injection of IR800CW-tagged P1, P2, or P3 (10 mg/kg), and *ex vivo* fluorescence images of tumor and major organs harvested at 24 h after administration. (c) Fluorescence images of EO771 tumor tissues excised at 24 h after treatment with IR800CW-tagged P1, P2 or P3. (d) Quantification of total radiation efficiency (near infrared fluorescence signal) of tumor and major organs at 24 h after treatment (n=3, mean±standard deviation, SD); unpaired Student's *t* test in comparison with P1. (e) Time course of polypeptide concentrations in blood plasma after intravenous administration of IR800CW-tagged P1, P2, or P3 (10 mg/kg, n=3, mean±SD). Half-life and area under the curve (AUC) values were calculated by GraphPrism. (f, g) Measurement of $IR800CW^{+}$

fluorescence signals in (f) $CD45^+$ cells (leukocytes), $CD45^-$ $EpCAM^+$ (EO771 tumor cells), and (g) immune cell subtypes (macrophages: $CD11b^+CD11c^-F4/80^+$, dendritic cells [DCs]: $CD11c^+$MHC-$II^+F4/80^-$, neutrophils: $CD11b^+CD11c^-$MHC-II^-Gr1^+, T cells: $CD3^+$, NK cells: $CD3^-NKp46^+NK1.1^+$) by flow cytometry of tumors 24 after treatment with IR800CW-tagged P1, P2, or P3 (10 mg/kg). Unpaired two-tailed Student's *t* test in comparison with $CD45^+$ for (f) or to P1 for (g). (h) Immunofluorescence images show that IR800CW-tagged P1 accumulates in macrophages and DCs within tumor microenvironments to a greater extent than IR800CW-tagged P2 or P3; scale bar, 15 μm (i) Timeline of treatment with P1, P2, and P3 in EO771 tumor-bearing mice. (j) P1 suppressed tumor growth and extended survival of tumor-bearing mice compared with P2 or P3 (n=5, mean±SD), unpaired Student's *t* test in comparison with P1 at day 28 after tumor inoculation for tumor growth curves; log-rank (Mantel-Cox) test for Kaplan-Meier survival curves.

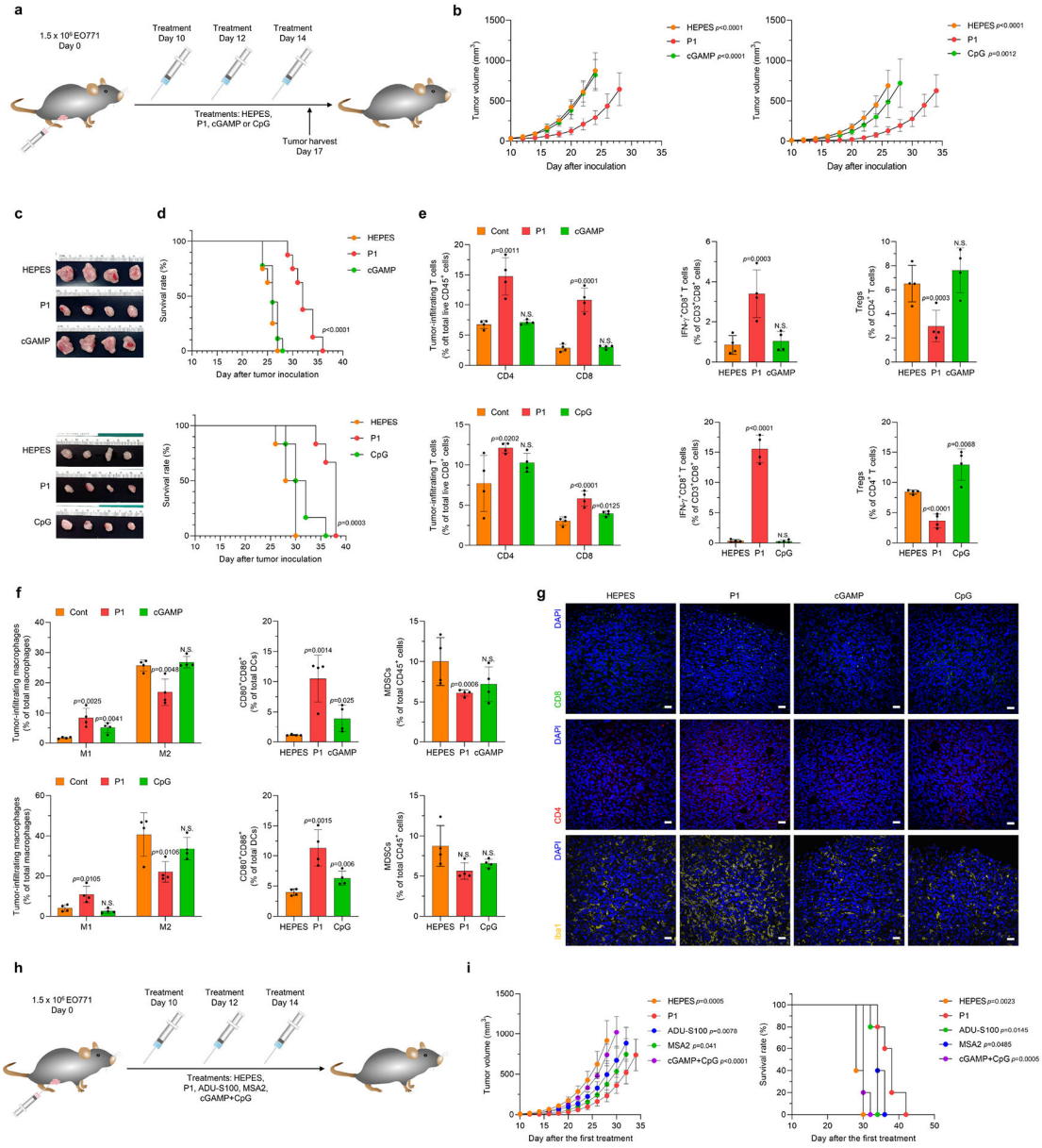

Fig. 2. P1 inhibits tumor growth and extends survival in tumor-bearing mice.

(a) Timeline of intravenous treatments (10 mg/kg for P1, cGAMP, and CpG). (b) Growth curves for EO771 tumors in mice after the indicated treatments. (For tumor inhibition study with HEPES, P1, and cGAMP: n=8 biologically independent mice for each group; unpaired Student's *t* test in comparison to P1 at day 24 after tumor inoculation. For tumor inhibition study with HEPES, P1, and CpG: n=6 biologically independent mice for each group; unpaired Student's *t* test in comparison to P1 at day 26 after tumor inoculation, mean±SD). (c) Tumor tissues from each treatment group were excised 2 days after the last treatment. (d) Kaplan-Meier survival curves of EO771 tumor-bearing mice show that P1 extended survival; log-rank (Mantel-Cox) test. (e) P1 increased tumor-infiltrating T cells and IFN-γ^+CD8$^+$ T cells but reduced Tregs (Foxp3$^+$CD25$^+$CD4$^+$ T cells) (n=4, mean±SD). Tumor-infiltrating lymphocytes were harvested 2 days after the last treatment. (f) Flow

cytometry of tumor-infiltrating M1 ($CD80^+CD86^+CD206^-$) and M2 ($CD80^-CD206^+$) macrophages ($CD11b^+CD11c^-F4/80^+MHC\text{-}II^-$), DCs ($CD11c^+F4/80^-MHC\text{-}II^+$) and MDSCs ($CD11b^+CD11c^-F4/80^-MHC\text{-}II^-Gr\text{-}1^+$) show that P1 activated innate immune responses in the tumor microenvironment (n=4, mean±SD); unpaired Student's *t* test in comparison to Cont. (g) Immunohistological staining of tumor tissues stained for $CD4^+$, $CD8^+$, and $Iba1^+$ (scale bar, 30 μm). (h) Timelines for systemic treatments [10 mg/kg for P1, ADU-S100 (a synthetic STING agonist with thiol esters), MSA-2 (non-nucleotide STING agonist); or 10 mg/kg cGAMP+10 mg/kg CpG for cGAMP+CpG]. (i) P1 treatment suppressed tumor growth and increased survival period of EO771 tumor-bearing mice to a comparable extent as MSA-2 and to a greater extent than the other treatments (n=5, mean±SD), Student's *t* test in comparison with P1 at Day 26 after tumor inoculation for tumor growth curves; log-rank (Mantel-Cox) test in comparison with P1.

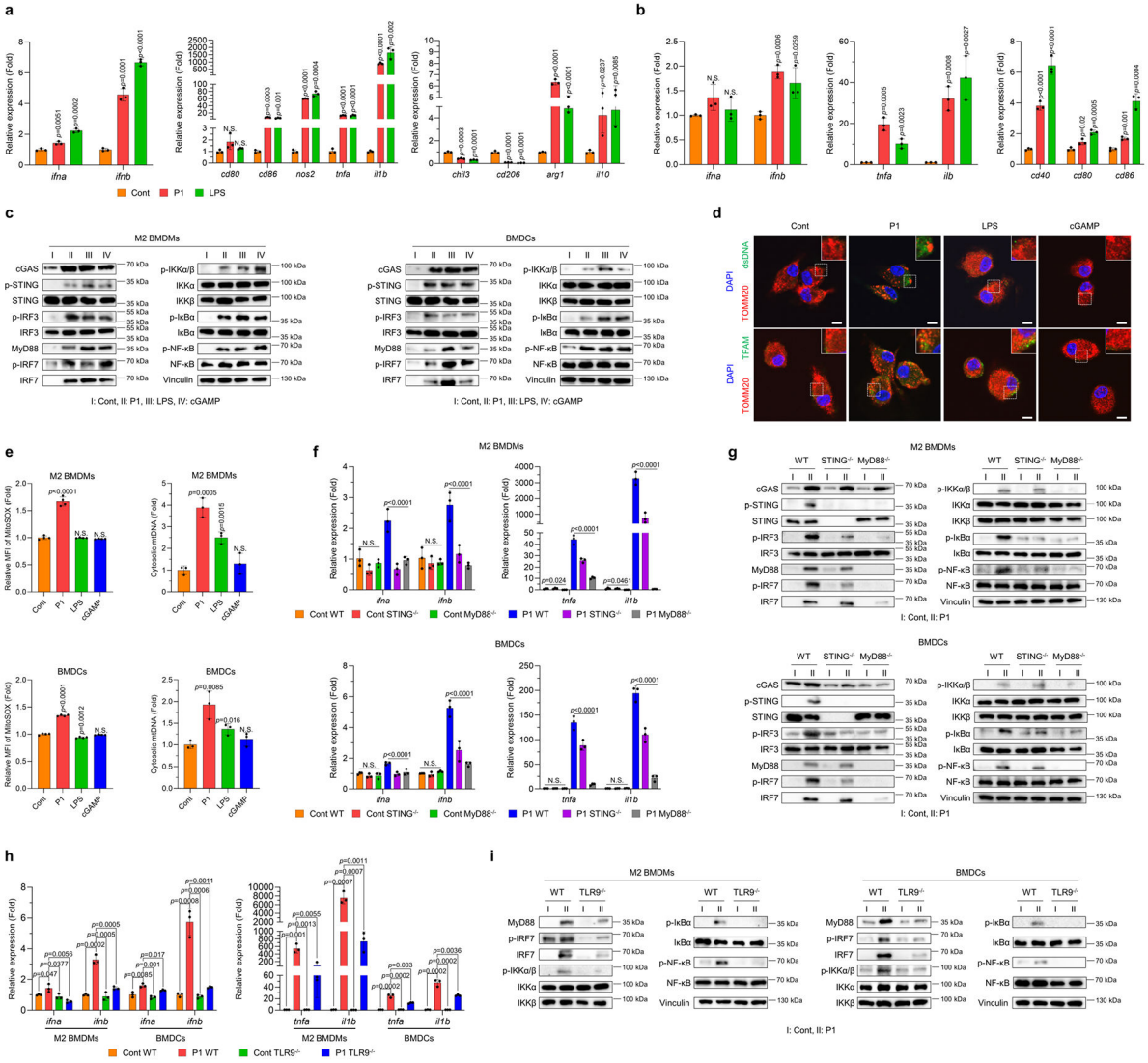

Fig. 3. P1 activates innate immune sensors by releasing mtDNA.

(a) P1 upregulated the expression of type I interferon (IFN)-related and M1-associated genes, but reduced that of M2-related genes, in M2 macrophages, as determined by quantitative reverse transcription polymerase chain reaction (RT-qPCR) (n=3, mean±SD); unpaired Student's *t* test in comparison to control (Cont). (b) P1 treatment of BMDCs increased the expression of genes for type I IFNs, pro-inflammatory cytokines and co-stimulatory molecules on DC surfaces (n=3, mean±SD). (c) Western blots show that P1 stimulated cGAS-STING, MyD88, and NF-κB pathways in M2 BMDMs and BMDCs. (d) P1 triggered release of transcription factor A, mitochondrial (TFAM) and double-stranded DNA (dsDNA) from mitochondria in M2 macrophages, as visualized by confocal laser scanning microscopy (scale bar 7.5 μm). (e) Treatment of M2 BMDMs and BMDCs with P1 led to increased levels of mitochondrial ROS, as evaluated by flow cytometry (n=4, mean±SD) and promoted mtDNA release, as quantified by RT-qPCR (n=3, mean±SD); unpaired Student's *t* test in comparison to Cont. (f) P1 treatment led to increased expression of genes encoding type I IFNs and pro-inflammatory cytokines in wild-type APCs, but

not in STING$^{-/-}$ or MyD88$^{-/-}$ ones (n=3, mean±SD); Ordinary one-way ANOVA. (g) Western blots of proteins related to cGAS-STING, MyD88, and canonical NF-κB pathways in STING$^{-/-}$ or MyD88$^{-/-}$ APCs. (h) TLR9 deficiency in M2 macrophages and BMDCs treated with P1 reduced the expression of genes encoding type I IFNs and pro-inflammatory cytokines (n=3, mean±SD); unpaired Student's *t* test in comparison to Cont. (i) TLR9-depleted APCs downregulated the MyD88-IRF7 and canonical NF-κB axes.

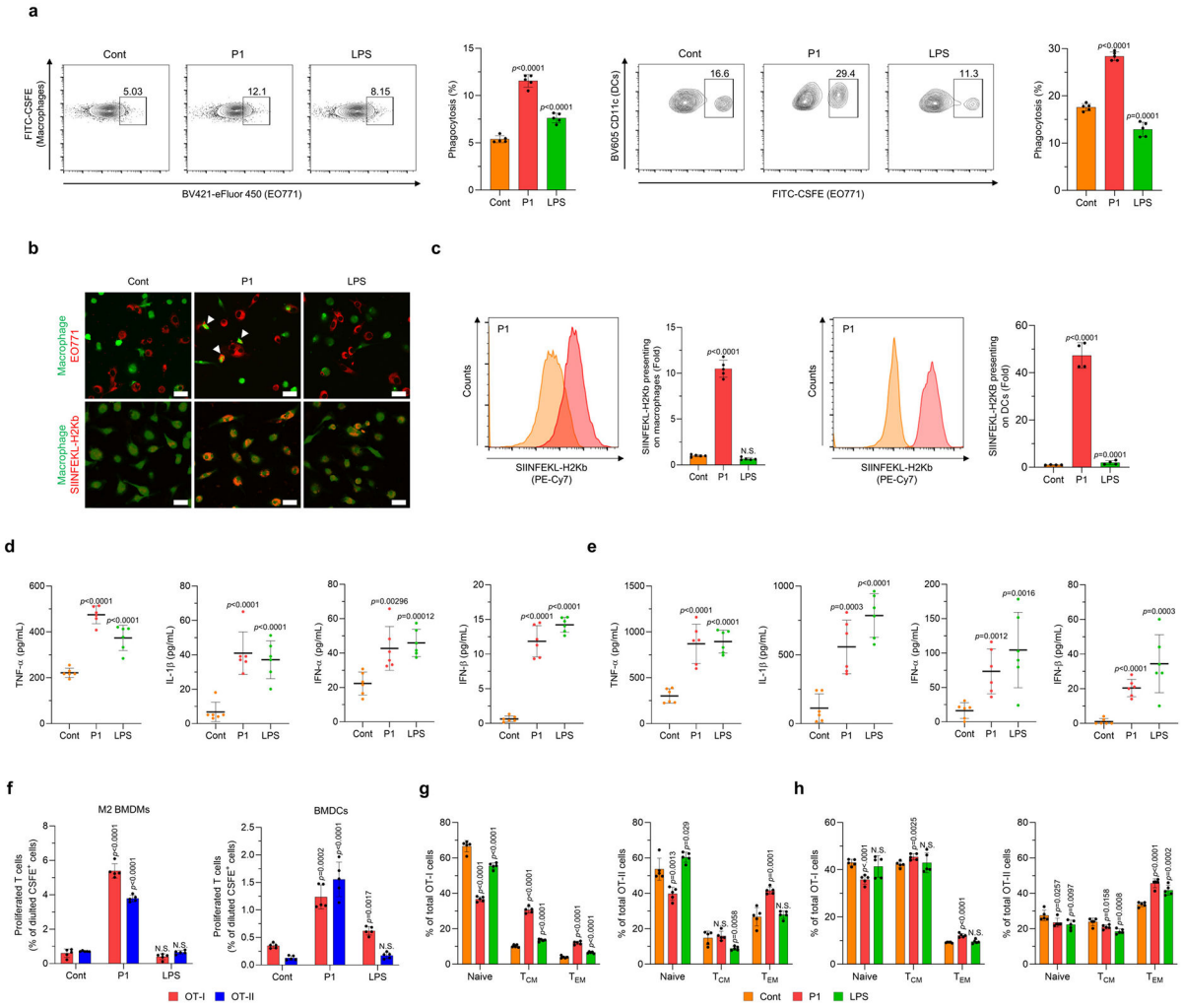

Fig. 4. P1 enhances the phagocytosis of cancer cells and the priming of antigen-specific T cells by professional antigen-presenting cells.

(a) P1 increased the phagocytic activity of M2 bone marrow-derived macrophages BMDMs and BMDCs, as evaluated by flow cytometry (n=5, mean±SD). (b) Macrophages promoted the phagocytosis of EO771 cells (white arrows) and cross-presentation of ovalbumin (OVA) peptide (SIINFEKL-H2Kb) on their surface, as visualized by confocal laser scanning microscopy; scale bar 20 μm. (c) P1 promoted cross-presentation of SIINFEKL-H2Kb peptides on the surfaces of M2 BMDMs (n=5, mean±SD) and BMDCs (n=4, mean±SD), as assessed by flow cytometry to normalize mean fluorescence intensity of SIINFEKL-H2Kb peptides; unpaired Student's *t* test in comparison to Cont. (d,e) P1 increased the production of pro-inflammatory cytokines (TNF-α, IL-1β) and type I interferons (IFN-α and IFN-β) in co-cultures of EO771 cancer cells with (d) M2 BMDMs or (e) BMDCs (n=6, mean±SD). (f) P1 induced the proliferation of both $CD4^+$ and $CD8^+$ T cells isolated from transgenic OT-I and OT-II mice and co-cultured with P1-treated M2 BMDMs or BMDCs and cancer cells (n=5, mean±SD). (g,h) P1 activated T central memory (T_{CM}) and T effector memory (T_{EM}) subtypes of both $CD4^+$ and $CD8^+$ T cells with (g) M2 BMDMs or (h) BMDCs (n=5, mean±SD); unpaired Student's *t* test in comparison to Cont.

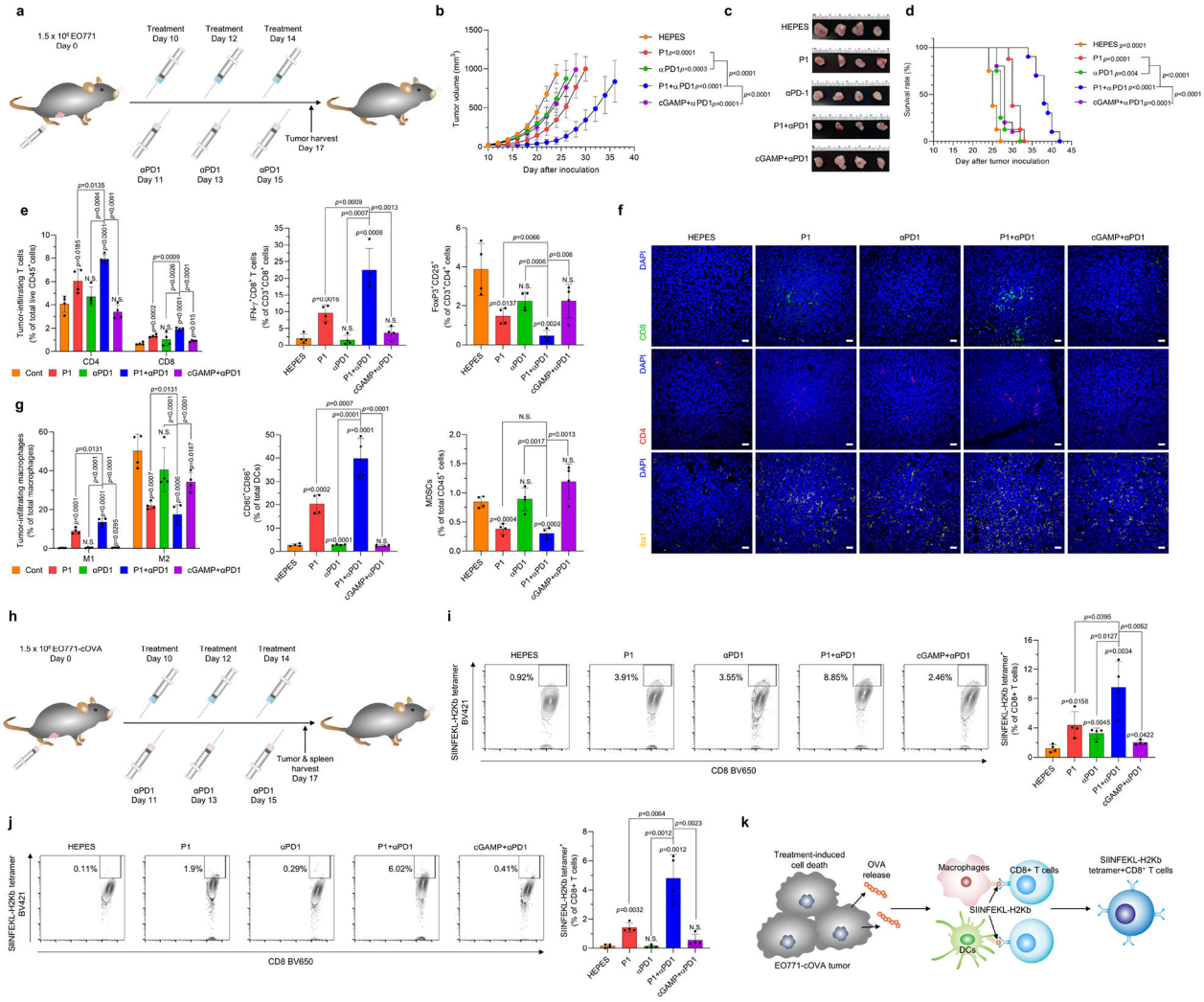

Fig. 5. P1 in combination with αPD1 has synergistic antitumor effects.

(a) Timeline for tumor establishment and administration of HEPES, P1, αPD1, P1+αPD1, and cGAMP+αPD1. (b) Growth curves for EO771 tumors from mice after the indicated treatments (n=8 for HEPES, P1, αPD1; n=10 for P1+αPD1, cGAMP+αPD1, mean±SD), unpaired Student's *t* test in comparison with HEPES or the indicated conditions at Day 24 after tumor inoculation. (c) Excised tumor tissues on day 17 from each group. (d) P1+αPD1 combination treatment prolonged survival in EO771 tumor-bearing mice; log-rank (Mantel-Cox) test in comparison to HEPES or the indicated conditions. (e) P1+αPD1 increased the population of tumor-infiltrating T cells and interferon (IFN)-γ^+CD8$^+$ T cells along with reducing the population of Tregs, as evaluated by flow cytometry (n=4, mean±SD). (f) Immunofluorescence stains of tumor-infiltrating T cells and Iba1$^+$ cells show that the combination treatment modulated the tumor microenvironments; scale bar, 30 μm. (g) P1+αPD1 combination treatment promoted M1 macrophage polarization and maturation of DCs while decreasing the population of MDSCs, as verified by flow cytometry (macrophages: CD11b$^+$CD11c$^-$F4/80$^+$ MHC-II$^-$, DCs: CD11c$^+$F4/80$^-$MHC-II$^+$, MDSCs: CD11b$^+$CD11c$^-$F4/80$^-$MHC-II$^-$Gr-1$^+$, M1: CD80$^+$CD86$^+$CD206$^-$ macrophages,

M2: $CD80^{-}CD206^{+}$ macrophages) (n=4, mean±SD). Unpaired Student's *t* test in comparison to 'Cont' or the indicated condition. (h) Timeline for tumor inoculation with EO771-cOVA and the indicated treatments. P1+αPD1 increased SIINFEKL-H2Kb $tetramer^{+}CD8^{+}$ T cells (i) within the tumor microenvironment and (j) in spleen (n=4, mean±SD); unpaired Student's *t* test in comparison with HEPES or the indicated conditions. (k) Schematic illustrating the mechanism of SIINFEKL-H2Kb $tetramer^{+}$ $CD8^{+}$ T cell expansion

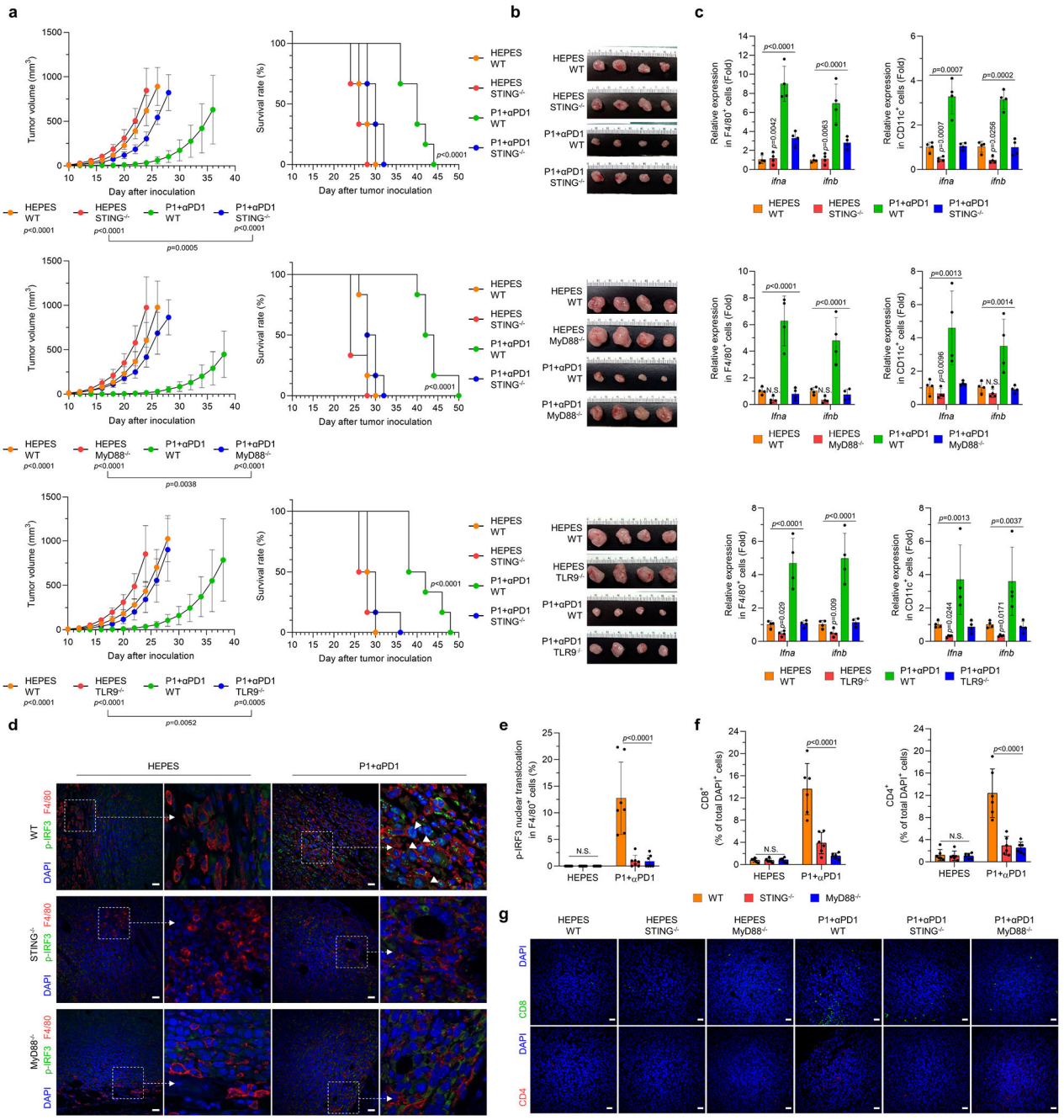

Fig. 6. Activation of STING and TLR9-MyD88 is essential for P1+αPD1–induced immune responses.

(a) Knockout of STING, MyD88, and TLR9 abrogated the antitumor effect of combined P1+αPD1 treatment and curtailed survival of EO771 tumor-bearing mice (n=6 for all experimental arms except for P1+αPD1 WT [n=8] in studies of tumor inhibition, mean±SD); unpaired Student's *t* test in comparison with P1+αPD1 WT or the indicated conditions at day 24 after tumor inoculation for tumor growth graphs; log-rank (Mantel-Cox) test for Kaplan-Meier survival curves. (b) Harvested tissues from WT, STING$^{-/-}$, MyD88$^{-/-}$, or TLR9$^{-/-}$ tumors on day 16 after treatment with HEPES or P1+αPD1.

(c) P1+αPD1 increased the production of *ifna* and *ifnb* in tumor-homing macrophages ($F4/80^+$) and in tumor-homing DCs ($CD11c^+$) by stimulating STING and TLR9-MyD88 (n=4, mean±SD); ordinary one-way ANOVA or unpaired Student's *t* test in comparison with P1+αPD1 knockout mouse strains. (d) Immunofluorescence images show that P1+αPD1 promoted phosphorylation of IRF3 (p-IRF3) and its nuclear translocation (white arrow) in tumor-homing macrophages by activating STING and MyD88; scale bar, 30 μm. (e,f) Quantification of nucleus-translocating (e) $p\text{-}IRF3^+$ macrophages and (f) tumor-infiltrating $CD4^+$ and $CD8^+$ T cells (n=7 independent images for p-IRF3, n=6 independent images for CD4 and CD8, mean±SD); ordinary one-way ANOVA. (g) Immunofluorescence staining of $CD8^+$ and $CD4^+$ T cells in EO771 tumors from WT, $STING^{-/-}$, and $MyD88^{-/-}$ mice; scale bar, 30 μm. Cells shown in the immunofluorescence images were counted with ImageJ.

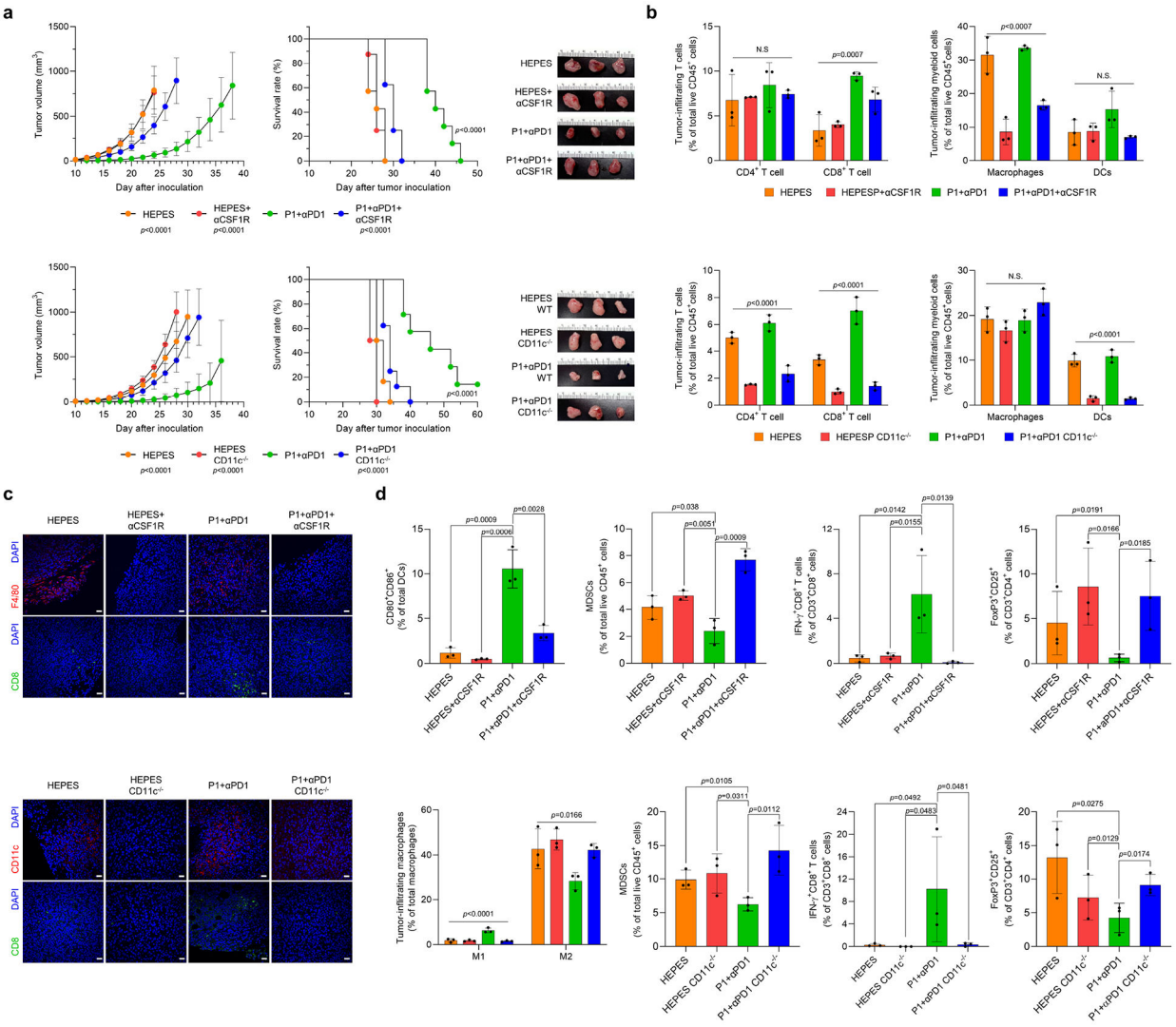

Fig. 7. Activation of innate immunity is indispensable for the antitumor effect conferred by P1+αPD1.

(a) Depletion of macrophages (by αCSF1R) and dendritic cells (DCs) (by diphtheria toxin) in *CD11c-DTR/GFP* mice abolished the antitumor effect of P1+αPD1 and shortened the survival of EO771 tumor-bearing mice (for the macrophage-depletion study, n=6 for HEPES; n=7 for P1+αPD1; n=8 for HEPES αCSF1R, P1+αPD1 αCSF1R; for the DC-depletion study, n=6 for HEPES, HEPES CD11c$^{-/-}$; n=7 for P1+αPD1; n=8 for P1+αPD1 CD11c$^{-/-}$, mean±SD); unpaired Student's *t* test in comparison with P1+αPD1 at Day 24 for macrophage-depleted study and at Day 28 for DC-depleted study, log-rank (Mantel-Cox) test for Kaplan-Meier survival curve. (b) Immune profile of tumor-infiltrating lymphocytes confirms depletion of macrophages or DCs and inhibition of T cell-infiltration into the tumor (n=3, mean±SD); Ordinary one-way ANOVA. (c) Immunofluorescence images show that depletion of macrophages and DCs prevented the recruitment of CD8^{+}, F4/80^{+} or CD11c^{+} cells into the tumor (scale bar, 30 μm). (d) Subtype profiles of tumor-infiltrating T cells and myeloid cells in EO771 tumors show that depletion of macrophages or DCs

blocked remodulation of the tumor microenvironments toward an immunostimulatory mode (n=3, mean±SD).

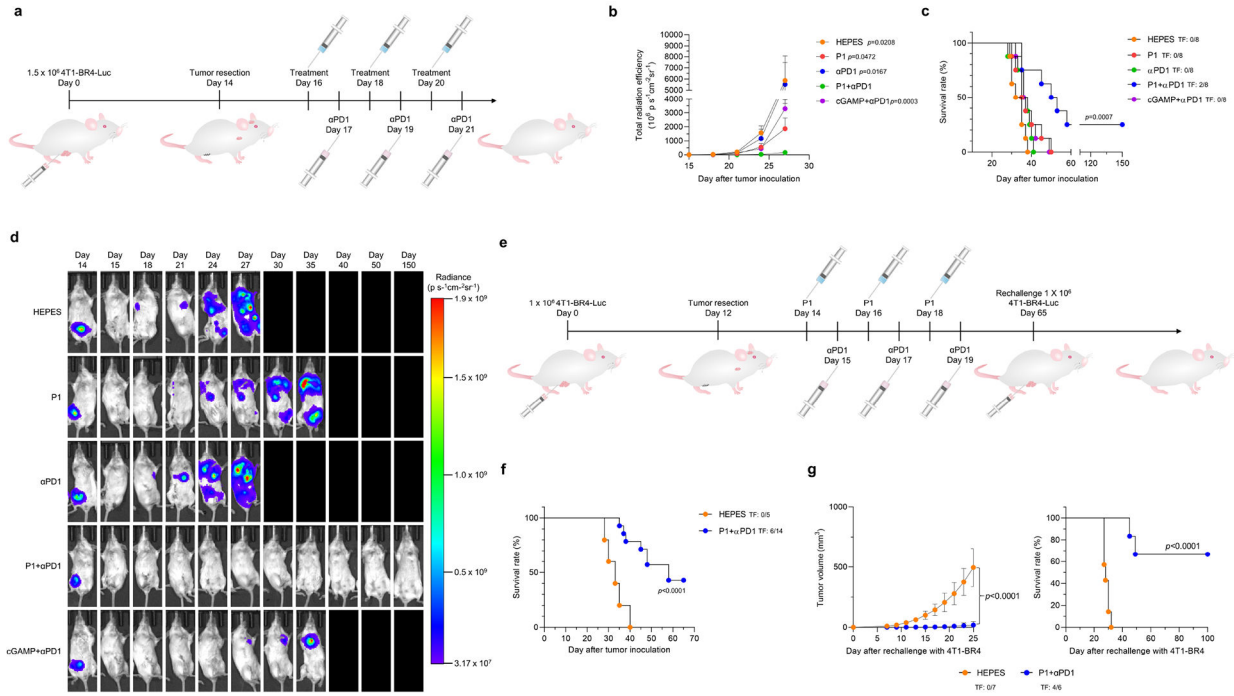

Fig. 8. P1 plus αPD1 suppresses the metastasis of aggressive breast tumors.

(a) Timeline illustrating resection of 4T1-BR4 breast tumors followed by treatment with P1+αPD1 to inhibit spontaneous metastasis in this model. (b) Quantification of luminescence signals of the whole body (n=8, mean±standard error of the mean), unpaired Student's t test in comparison with P1+αPD1 on day 27 after tumor inoculation. (c) Kaplan-Meier survival curves of mice with 4T1-BR4 tumor metastases (n=8 for all treatment groups), log-rank (Mantel-Cox) test. TF, tumor-free. (d) Representative *in vivo* bioluminescence images for monitoring metastasis of 4T1-BR4-Luc breast tumor cells after tumor resection from one of the eight independent mice. (e) Treatment schedule for tumor re-challenge with 4T1-BR4 breast tumor cells after treatments with P1+αPD1. (f) Kaplan-Meier survival curves of mice with 4T1-BR4 tumor metastases (n=5 for HEPES, n=14 for P1+αPD1), log-rank (Mantel-Cox) test. (g, f) Treating immunized mice with P1+αPD1 led to (g) suppressed re-occurrence of tumor establishment, thus increasing the mouse survival time (n=7 for naïve, n=6 for P1+αPD1), unpaired Student's *t* test in comparison with naïve mice for tumor growth curve on day 25; log rank (Mantel-Cox) test for Kaplan-Meier survival curve. TF, tumor-free.